

# Multi-view Surface Reconstruction Using Normal and Reflectance Cues

Robin Bruneau<sup>1\*†</sup>, Baptiste Brument<sup>2\*†</sup>, Yvain Quéau<sup>3</sup>, Jean Mélou<sup>2, 4</sup>,  
François Bernard Lauze<sup>5</sup>, Jean-Denis Durou<sup>2</sup>, Lilian Calvet<sup>6</sup>

<sup>1</sup>DQBM, University of Zurich, Switzerland.

<sup>2</sup>IRIT, UMR CNRS 5505, Université de Toulouse, France.

<sup>3</sup>GREYC, CNRS, UNICAEN, ENSICAEN, Normandie Université, France.

<sup>4</sup>FittingBox, Toulouse, France.

<sup>5</sup>DIKU, University of Copenhagen, Denmark.

<sup>6</sup>ROCS, University of Zurich, OR-X, Balgrist University Hospital, Switzerland.

\*Corresponding author(s). E-mail(s): [robin.bruneau@uzh.ch](mailto:robin.bruneau@uzh.ch); [baptiste.brument@irit.fr](mailto:baptiste.brument@irit.fr);  
Contributing authors: [yvain.queau@ensicaen.fr](mailto:yvain.queau@ensicaen.fr); [jean.melou@irit.fr](mailto:jean.melou@irit.fr); [francois@di.ku.dk](mailto:francois@di.ku.dk);  
[jean-denis.durou@irit.fr](mailto:jean-denis.durou@irit.fr); [lilian.calvet@balgrist.ch](mailto:lilian.calvet@balgrist.ch);

†These authors contributed equally to this work.

## Abstract

Achieving high-fidelity 3D surface reconstruction while preserving fine details remains challenging, especially in the presence of materials with complex reflectance properties and without a dense-view setup. In this paper, we introduce a versatile framework that incorporates multi-view normal and optionally reflectance maps into radiance-based surface reconstruction. Our approach employs a pixel-wise joint re-parametrization of reflectance and surface normals, representing them as a vector of radiances under simulated, varying illumination. This formulation enables seamless incorporation into standard surface reconstruction pipelines, such as traditional multi-view stereo (MVS) frameworks or modern neural volume rendering (NVR) ones. Combined with the latter, our approach achieves state-of-the-art performance on multi-view photometric stereo (MVPS) benchmark datasets, including DiLiGenT-MV, LUCES-MV and Skoltech3D. In particular, our method excels in reconstructing fine-grained details and handling challenging visibility conditions. The present paper is an extended version of the earlier conference paper by Brument et al. (in Proceedings of the IEEE/CVF Conference on Computer Vision and Pattern Recognition (CVPR), 2024), featuring an accelerated and more robust algorithm as well as a broader empirical evaluation. The code and data relative to this article is available at <https://github.com/RobinBruneau/RNb-NeuS2>.

**Keywords:** 3D Surface Reconstruction, Neural Volume Rendering, Multi-view Photometric Stereo, Multi-view Normal Integration.

# 1 Introduction

Surface reconstruction is essential in various fields, including cultural heritage preservation, medical imaging, virtual and augmented reality, digital twinning, and content creation for games and film production. Despite significant advancements, the performance of state-of-the-art surface reconstruction methods remains highly dependent on scene characteristics, notably the presence of fine-scale geometric details and the possibly complex reflectance properties of the surface.

The recovery of fine-grained structures is a long-standing bottleneck in 3D surface reconstruction. Traditional multi-view stereo (MVS) methods (Furukawa and Ponce, 2007; Schönberger et al, 2016) often produce overly smoothed surfaces, struggling with sharp edges and intricate geometries (Seitz et al, 2006; Furukawa et al, 2015). Recent neural approaches have advanced surface reconstruction in this direction by shifting from local, patch-based optimization to global, pixel-wise optimization (Yariv et al, 2020, 2021; Oechsle et al, 2021; Wang et al, 2021b). Notably, methods such as HF-NeuS (Wang et al, 2022b), PET-NeuS (Wang et al, 2023b), NeuS2 (Wang et al, 2023a), and Neuralangelo (Li et al, 2023) excel in capturing fine surface details – at least, when the density of viewpoints is high (Brument et al, 2024; Logothetis et al, 2024).

On the other hand, approaches leveraging multi-light information have demonstrated strong performance in recovering intricate surface geometries, even in the sparse-view scenario. This is after all the principle of photometric stereo (PS), which achieves monocular 2.5D reconstruction under the form of a normal map, under varying illumination (Woodham, 1980). Several recent multi-view, multi-light setups such as SuperNormal (Cao and Taketomi, 2024) or our previous work RNb-NeuS (Brument et al, 2024) thus employ PS at each viewpoint, before resorting to multi-view normal integration for complete 3D surface reconstruction.

Apart from fine details, complex materials (metallic, specular, translucent, rough, etc.) represent another challenge due to the strong view-dependence of reflectance – hence of radiance, which breaks the brightness consistency assumption upon which MVS is fundamentally based (Seitz et al, 2006; Furukawa et al, 2015).

Although recent single-image approaches have demonstrated promising results in reconstructing accurate surface normals even for complex materials, by leveraging inductive biases and diffusion mechanisms (Bae and Davison, 2024; Ye et al, 2024) within vision transformers (ViTs) (Kolesnikov et al, 2021), the most natural way to cope with complex materials remains active illumination i.e., PS.

The most recent deep learning-based PS techniques, also based on ViTs, indeed recover detailed surface normal maps and fine geometric structures even for highly complex materials, both when the illumination is calibrated (Wei et al, 2025) or when it is unknown and possibly spatially-varying (so-called “universal” PS setup (Ikehata, 2022b, 2023; Hardy et al, 2024)). Besides, some of these methods (Ikehata, 2022b, 2023) even extend beyond normal estimation by estimating reflectance properties such as diffuse colour, roughness, or metalness, thereby enabling virtual relighting applications.

Motivated by the strong performance of recent PS methods in estimating detailed surface normals and reflectance properties, the present work proposes a multi-view surface reconstruction approach designed to inherit these advancements. Our approach follows a two-stage decomposition strategy that proves effective even without dense multi-view inputs. Specifically, we first estimate per-view surface normals (and optionally reflectance properties) from multi-light input data, and subsequently reconstruct a surface that best aligns with these estimates across multiple views.

This paper builds upon and significantly extends our previous conference publication (Brument et al, 2024), where the foundational concepts of this two-stage approach were introduced. Therein, we presented the key idea to re-parametrize normal and reflectance priors into simulated radiance values on a per-pixel basis, facilitating seamless incorporation into existing surface reconstruction pipelines, notably neural volume rendering (NVR) frameworks based on signed distance functions (SDF). This innovative way to perform multi-view normal (and reflectance) integration yields a state-of-the-art multi-view photometric stereo (MVPS) technique, summarized in Figure 1, which we evaluated on

the DiLiGenT-MV dataset (Li et al, 2020) using the SDM-UniPS method (Ikehata, 2023) for normal and reflectance estimation.

In the present extension, we substantially improve upon this initial contribution in terms of speed, robustness, versatility, and evaluation. In particular:

- We implement our approach within the NeuS2 framework (Wang et al, 2023a), achieving a 100× speedup compared to our original implementation (see Section 5.5).
- We improve the robustness of our approach to reflectance singularities by introducing reflectance embedding (see Section 5.4).
- In addition to volume rendering, we validate our re-parametrization in a traditional patch-based MVS framework, demonstrating both its broad applicability and its ability to achieve *exact* integration in a noiseless setup (see Section 4).
- An alternative use case is explored, by substituting photometric stereo-estimated normals with ones derived from dense MVS under fixed illumination (Schönberger et al, 2016), thereby improving fine-structure reconstruction on the DTU dataset (Jensen et al, 2014) (see Section 6.4).
- A much deeper evaluation of our MVPS solution is conducted (see Section 6.2), notably under a sparse-view setup and on additional benchmarks such as LUCES-MV (Logothetis et al, 2024) and Skoltech3D (Voynov et al, 2023), using various PS results as input (Ikehata, 2023; Hardy et al, 2024). We also compare our results against the very recent SuperNormal method (Cao and Taketomi, 2024), which happens to be a special case of our approach (see Section 5.3).

The rest of this article is organized as follows. We first review the relevant literature in Section 2. Then, we show in Section 3 how to jointly re-parametrize normal and reflectance data into simulated radiance values. We embed this re-parametrization in a traditional MVS framework in Section 4, to demonstrate the feasibility of exact surface reconstruction from normals and reflectance cues. To ensure robustness, in Section 5 we then turn our attention to replacing this framework by a volume rendering one based on neural implicit surfaces. Extensive experiments validating the proposed approach are then conducted in

Section 6, before our conclusions are drawn in Section 7.

## 2 Related Work

With our normal and reflectance integration approach in mind, let us review estimation of normals, of reflectance, and integration techniques.

### 2.1 Normal Estimation

Normal maps carry out high-frequency geometric information. Their estimation is achieved differently depending on the amount of input data.

**Single-image normal estimation** is highly beneficial for 3D scene reconstruction, since it preserves local geometry without metric ambiguity (Yu et al, 2022; Wang et al, 2022a). Recent approaches predominantly leverage learning-based methodologies (Li et al, 2015; Wang et al, 2015; Qi et al, 2018, 2020; Liao et al, 2019; Do et al, 2020; Bae et al, 2022; Yang et al, 2024). However, direct training on real data remains challenging, as normal labels cannot be directly captured by current sensor technology. Typically, normals are thus inferred from depth maps (Silberman et al, 2012; Eigen and Fergus, 2015), but inaccuracies persist despite various correction strategies (Bae et al, 2021; Long et al, 2024). Therefore, the most recent works employed large-scale datasets of synthesized data such as OmniData (Eftekhari et al, 2021; Kar et al, 2022), along with smart architectural choices, e.g. per-pixel ray direction modelling in DSINE (Bae and Davison, 2024) or ViTs and diffusion models in StableNormal (Ye et al, 2024).

**Photometric stereo** (Woodham, 1980), on the other hand, is also a monocular technique yet it analyzes multiple images captured under varying lighting. The historical inverse problem-based PS approach, which fits normals and reflectance to a physics-based image formation model, has been employed in the calibrated (known illumination) scenario (Goldman et al, 2009; Wu et al, 2011; Shi et al, 2012; Ikehata et al, 2012; Ikehata and Aizawa, 2014), in the uncalibrated one (Hayakawa, 1994; Chandraker et al, 2005; Alldrin et al, 2007; Favaro and Papadimitri, 2012; Quéau et al, 2017), as well as under unknown and spatially-varying lighting (Basri et al, 2007; Quéau et al, 2015; Mo et al, 2018; Haefner et al, 2019; Guo et al, 2021). However, switching from the inverse

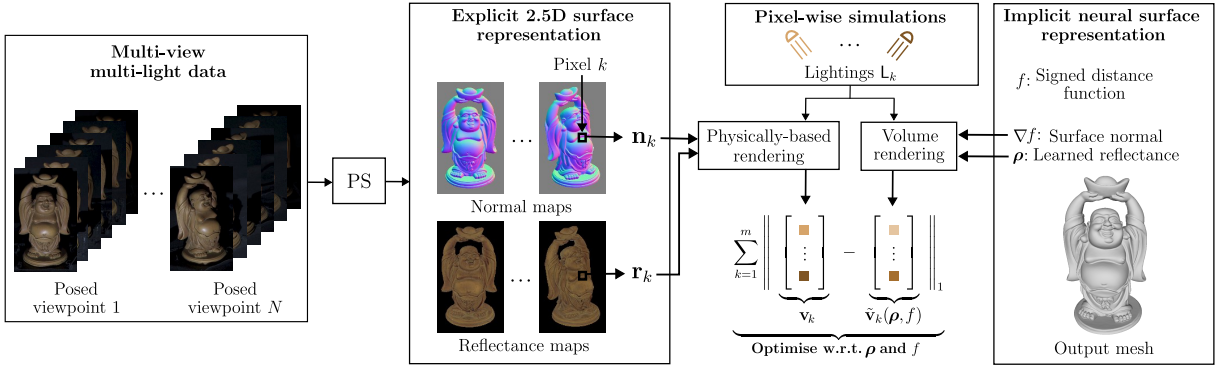


**Fig. 1:** Overview of the surface reconstruction pipeline “RNb-NeuS” proposed in Brument et al (2024). From multi-view multi-light data, photometric stereo (noted PS) first estimates per-view normal maps  $\{\mathbf{n}_k\}$  and optionally reflectance maps  $\{\mathbf{r}_k\}$ . These estimates are re-parametrized into radiance vectors  $\mathbf{v}_k = F(\mathbf{r}_k, \mathbf{n}_k, \mathbf{L}_k)$  via a physically-based rendering function  $F$  under simulated lightings  $\mathbf{L}_k$ . An implicit neural representation, consisting of a signed distance function  $f$  and a reflectance  $\rho$ , is then learned by minimising the discrepancy between  $\mathbf{v}_k$  and its volume-rendered counterpart  $\tilde{\mathbf{v}}_k(\rho, f)$ . The final surface mesh is extracted as the zero-level set of  $f$  after optimisation.

problem framework to the deep learning paradigm has recently revolutionized PS. Limitations of traditional physics-based models, especially regarding non-Lambertian effects, have thereby been addressed for both calibrated (Santo et al, 2017; Ikehata, 2018; Chen et al, 2018; Ikehata, 2022a; Wei et al, 2025) and uncalibrated PS (Taniai and Maehara, 2018; Chen et al, 2019, 2020; Kaya et al, 2021; Li and Li, 2022), and the most modern techniques make lighting context implicit, which both improves performances (Ju et al, 2025) and allows tackling “universal” (unknown and spatially-varying illumination) PS (Ikehata, 2022b, 2023; Hardy et al, 2024).

In **multi-view** single-light contexts, traditional methods, such as Colmap’s multi-view stereo (Schönberger et al, 2016), infer normal maps by analysing patch orientations (Bleyer et al, 2011). Differently, Calvet et al (2023) estimate normals from image grey level variations and use them in a slanted plane-sweeping algorithm. An alternative paradigm computes normals post-MVS by deriving them from depth maps, as demonstrated in RegSDF (Zhang et al, 2022), which utilizes depth from Vis-MVSNet (Zhang et al, 2023a). This depth-based normal estimation is MVS-method agnostic, applicable to both traditional (Furukawa and Ponce, 2007; Xu et al, 2022) and deep learning-driven methods (Yao et al, 2018; Gu et al, 2020; Zhang et al, 2023a).

## 2.2 Reflectance Estimation

Reflectance estimation involves recovering material properties defining surface-light interactions, which is critical for realistic relighting applications. As for normals, various methods can be employed depending whether a single image, multiple views, or multiple illuminations are available.

**Single-image inverse rendering** decomposes a single image into reflectance, geometry, and illumination using for instance multi-view self-supervision (Yu et al, 2020), or diffusion models to infer physically-based rendering (PBR) materials as in MaterialPalette (Lopes et al, 2024).

In **multi-view** frameworks, methods such as Ref-NeRF (Verbin et al, 2022) extend neural radiance fields (NeRF) to explicitly model reflections, improving the reconstruction of specular and glossy surfaces. Techniques like SHINOBI (Engelhardt et al, 2024) concurrently optimize geometry, reflectance, and illumination, enabling detailed relightable 3D assets. More recently, Diffusion-Renderer (Liang et al, 2025) provided a unified solution for high-quality normal and reflectance reconstruction from video sequences, by bridging monocular and multi-view estimation through diffusion models for neural inverse rendering.

Finally, the aforementioned **photometric stereo** technique is the only photographic technique designed for reflectance recovery (Woodham, 1980). In addition, multi-light approaches

offer two key advantages over single-light methods: they enhance reflectance estimation in shadowed regions (both self- and cast shadows) and improve robustness in areas affected by strong non-linearities, such as saturation in specular highlights, which shift across different lighting conditions.

### 2.3 Multi-view Normal Integration

Although individual normal maps carry valuable high-frequency geometry information, they may be inconsistent across varying viewpoints, making their fusion challenging.

In a **multi-view single-light** setting, MonoSDF (Yu et al, 2022) combined a normal and depth consistency loss derived from monocular predictions (Eftekhari et al, 2021) with a radiance constraint, a common approach in NeRF-like (Mildenhall et al, 2021) methods. Similarly, Gaussian Surfels (Dai et al, 2024) uses monocular normal predictions to constrain 3D Gaussian Splatting (3DGS) (Kerbl et al, 2023).

Yet, multi-view normal integration is much more studied under the prism of **multi-view photometric stereo**. This problem was first addressed by Hernández et al (2008), through the optimization of a loss combining a rendering term and a discrepancy between photometric stereo normals and the optimized mesh. Note that this first approach required neither prior knowledge of camera poses nor illumination conditions. Similarly, Park et al (2013, 2016) simultaneously estimated reflectance, normals, and illumination through uncalibrated PS, leveraging the 3D mesh normals to resolve ambiguities and refining surface details. Logothetis et al (2019) later formulated the problem within an SDF representation, achieving superior surface detail reconstruction compared to Park et al (2016). Further refinements were made by Li et al (2020), who enhanced a 3D mesh by propagating SfM points following the method of Nehab et al (2005), and validating their method through the introduction of the publicly available dataset “DiLiGenT-MV”.

**Neural surface reconstruction methods** have recently emerged as a promising alternative, by enforcing alignment between per-view normal maps and the gradient of a neural SDF. Kaya et al (2022) for instance constrained the

SDF optimization by CNN-PS normals (Ikehata, 2018) and MVS depths (Wang et al, 2021a), incorporating uncertainty measures to mitigate conflicts in predictions. Kaya et al (2023) further added a neural volume rendering loss, benefiting the latter’s robustness in handling various material types. This resulted in a multi-objective optimization comprising three loss terms. However, as in Kaya et al (2022), the reliance on uncertainty-based hyperparameter tuning did not fully resolve conflicts between objectives, leading to potential loss of fine-grained details. PS-NeRF (Yang et al, 2022) introduced a two-stage solution, where the first stage achieves multi-view normal integration by aligning surface gradients with SDPS-Net normals (Chen et al, 2019), and the second stage leverages UNISURF (Oechsle et al, 2021) to optimize geometry, reflectance and illumination, modelled by multi-layer perceptrons (MLPs). However, its reliance on the directional illumination assumption limited its generalizability. NPL-MVPS (Logothetis et al, 2025) relaxed this assumption by considering a near-light model, initially enforcing alignment between SDF gradients and UniMS-PS normals (Hardy et al, 2024), and subsequently processing to joint shape and reflectance optimization while considering both light attenuation and cast shadows. Most recently, SuperNormal (Cao and Taketomi, 2024) adopted a similar initialization approach to PS-NeRF and NPL-MVPS, utilizing SDM-UniPS normals (Ikehata, 2023), but significantly improved efficiency with multi-resolution hash encoding and directional finite differences, achieving nearly double the training speed.

In contrast to these prior methods, the novel approach we propose in the rest of this article formulates multi-view normal integration as a single-objective optimization problem, through joint re-parametrization of normals and reflectance. Let us now introduce this re-parametrization.

### 3 Reflectance and Normal Re-parametrization

Reflectance and surface normals traditionally represent distinct types of information: reflectance captures intrinsic photometric properties of surface materials, while normals describe the geometric orientation of surfaces. This inherent heterogeneity complicates their simultaneous optimization, typically necessitating separate processing steps, e.g., depth triangulation from multi-view data followed by the fusion of this depth information with normal maps using multi-objective optimization frameworks (Kaya et al, 2022, 2023).

To address this issue, we introduce a re-parametrization approach designed to unify surface normals and reflectance into homogeneous quantities, by mapping both of them to simulated radiance values under varying illumination conditions. This radiance-based parametrization enables a unified optimization reducing the need for additional regularization, commonly required in multi-objective contexts (Yu et al, 2022; Zhang et al, 2022), consequently enhancing consistency and computational efficiency. Indeed, a key motivation for radiance-based re-parametrization is its compatibility with existing photometric cost-minimization frameworks employed in classical multi-view stereo (Furukawa and Ponce, 2007; Schönberger et al, 2016) and neural volume rendering methods (Wang et al, 2021b; Yariv et al, 2021; Li et al, 2023). This incorporation facilitates optimization of photometric consistency across viewpoints or between input and rendered images.

#### 3.1 Input Data

Given a set of  $N$  viewpoints, we assume the availability of corresponding reflectance maps  $\mathbf{R}_i$  and normal maps  $\mathbf{N}_i$ , indexed by  $i \in \{1, \dots, N\}$ . Each viewpoint map comprises  $m$  pixels, indexed by  $k \in \{1, \dots, m\}$ , such that:

$$\mathbf{R}_i = \{\mathbf{r}_{i,k}\}_{k \in \{1, \dots, m\}}, \quad \mathbf{N}_i = \{\mathbf{n}_{i,k}\}_{k \in \{1, \dots, m\}}. \quad (1)$$

Therein, the reflectance for the  $k$ -th pixel in the  $i$ -th view is given by a parameter vector  $\mathbf{r}_{i,k} \in \mathbb{R}^q$  with dimension  $q$  corresponding to the specific reflectance model used, and the outward normal by a unit vector  $\mathbf{n}_{i,k} \in \mathbb{S}^2$ . The latter is expressed, using the known camera poses, in

world coordinates. If reflectance data is unavailable, simply setting  $\mathbf{r}_{i,k} = [1] \forall (i, k)$  allows our framework to be used exclusively for multi-view normal integration.

#### 3.2 Re-parametrization

Our re-parametrization approach transforms each couple of reflectance and normal vectors  $(\mathbf{r}_{i,k}, \mathbf{n}_{i,k})$  into a vector  $\mathbf{v}_{i,k}$  of homogeneous radiance values, simulated using a physically-based rendering (PBR) model:

$$\mathbf{v}_{i,k} = \mathbf{F}(\mathbf{r}_{i,k}, \mathbf{n}_{i,k}, \mathbf{L}_{i,k}), \quad (2)$$

with  $\mathbf{L}_{i,k} \in \mathbb{R}^{n \times l}$  the illumination conditions (chosen specifically for the  $k$ -th photosite of the  $i$ -th view) and  $\mathbf{F} : \mathbb{R}^q \times \mathbb{S}^2 \times \mathbb{R}^{n \times l} \rightarrow \mathbb{R}^{n \times q}$  the PBR function (for simplicity, the same model is used for all pixels). Here,  $l$  stands for the dimensionality of the light and  $n$  for that of the radiance representation, and both of them depend on the choice of a particular model.

While the general framework supports arbitrary PBR and illumination models, practical considerations regarding computational efficiency and implementation simplicity have guided our choice towards Lambertian reflectance and directional illumination. The former assumption simplifies reflectance to the albedo i.e.,  $\mathbf{r}_{i,k} \in \mathbb{R}$  or  $\mathbf{r}_{i,k} \in \mathbb{R}^3$ , depending on whether the images are in grey scale or RGB. The PBR function then reads:

$$\mathbf{F} : \mathbb{R}^q \times \mathbb{S}^2 \times \mathbb{R}^{n \times 3} \rightarrow \mathbb{R}^{n \times q} \\ (\mathbf{r}, \mathbf{n}, \mathbf{L}) \mapsto \mathbf{F}(\mathbf{r}, \mathbf{n}, \mathbf{L}) = \mathbf{L} \mathbf{n} \mathbf{r}^\top, \quad (3)$$

where the illumination vectors (in intensity and direction)  $\mathbf{l}_1, \dots, \mathbf{l}_n \in \mathbb{R}^3$  are stored row-wise in  $\mathbf{L}$ .

To ensure bijectivity of the mapping (2), we employ three distinct illumination vectors ( $n = 3$ ). Two additional constraints ensure bijectivity: (i) non-zero reflectance ( $\|\mathbf{r}_{i,k}\| \neq 0$ ), valid as long as the surface is not perfectly black, and (ii) linear independence of illumination directions (non-singular  $\mathbf{L}_{i,k}$ ). Under these conditions, the matrix  $\mathbf{L}_{i,k}$  is invertible. If  $q = 1$ , the inverse is given by  $\mathbf{r}_{i,k} = \frac{\|\mathbf{L}_{i,k}^{-1} \mathbf{v}_{i,k}\|}{\|\mathbf{L}_{i,k}^{-1} \mathbf{v}_{i,k}\|}$ ,  $\mathbf{n}_{i,k} = \frac{\mathbf{L}_{i,k}^{-1} \mathbf{v}_{i,k}}{\|\mathbf{L}_{i,k}^{-1} \mathbf{v}_{i,k}\|}$ . If  $q = 3$ , vectors  $\mathbf{n}_{i,k}$  and  $\mathbf{r}_{i,k}$  can be deduced from matrix  $\mathbf{L}_{i,k}^{-1} \mathbf{v}_{i,k} = \mathbf{n}_{i,k} \mathbf{r}_{i,k}^\top$  using SVD.

Employing  $n > 3$  illumination vectors may be interesting, especially when considering more advanced PBR models (including specularity, roughness, or anisotropy) or in uncertain input scenarios, yet at the expense of bijectivity. We leave this avenue for future research.

### 3.3 Optimal Illumination Directions

Although the mapping  $(\mathbf{r}_{i,k}, \mathbf{n}_{i,k}) \mapsto \mathbf{v}_{i,k}$  is bijective for any non-singular illumination matrix  $\mathbf{L}_{i,k}$ , not all choices are equally adapted to our task. Indeed, the input reflectances and normals being prone to estimation errors, radiance values can be considered “noisy”. Since we will next invert the PBR model from these noisy values, the conditioning of the illumination matrices will have a substantial impact on the accuracy of the numerical inversion.

We therefore chose the widely accepted configuration suggested by [Drbohlav and Chantler \(2005\)](#), which employs three illumination configurations with equal intensity, and directions spaced equally by  $120^\circ$  in azimuth, each with a constant slant of  $54.74^\circ$  relative to the normal vector  $\mathbf{n}_{i,k}$ . Alternative illumination arrangements, such as those embedded in SuperNormal ([Cao and Taketomi, 2024](#)), will be assessed in Section 5.3.

In addition to numerical considerations, this particular choice also avoids self-shadowing, namely negative dot products between normals and illumination vectors. Nevertheless, our method could accommodate non-physical negative radiance as long as the rendering function of the downstream reconstruction technique is consistent. In the next section, we explore a first possibility for the latter downstream technique, which is surface sweeping.

## 4 Surface Sweeping-based 3D Reconstruction

As a first proof of concept, let us now apply the re-parametrization we proposed in Section 3 to triangulation-based MVS, a method that estimates the depth for each pixel in a reference view by maximizing the photometric consistency in other (control) views. In particular, we will show that by leveraging the information provided by the normals, plane sweeping-based algorithms ([Collins, 1996](#)) can be turned into an *exact*

surface sweeping-based method for integrating multi-view normal data, eliminating the inherent approximation errors due to local planar surface assumptions, e.g., fronto-parallel or slanted patches ([Furukawa and Ponce, 2007](#); [Bleyer et al, 2011](#); [Schönberger et al, 2016](#)).

### 4.1 Objective Function

Our aim is to compute depth values for all pixels in the first view, considered as reference. Without loss of generality, this reference camera frame aligns with the world coordinate system. The  $N-1$  other views then serve as control views for enforcing multi-view consistency on the reflectance and normals. The optimization of multi-view consistency is usually carried out locally, by splitting the pixels of the reference view into patches  $\mathcal{P} \subset \mathbb{R}^2$  containing  $m_{\mathcal{P}}$  pixels. We will denote by  $\{\mathbf{v}_{1,j}\}_{j \in \{1, \dots, m_{\mathcal{P}}\}}$  the re-parametrized reflectance and normals over this patch. Formulated in terms of this re-parametrization, finding the depth of the patch centre that maximizes multi-view consistency of reflectance and normal maps amounts to solving:

$$\min_{z>0} \sum_{i=2}^N \sum_{j=1}^{m_{\mathcal{P}}} \|\mathbf{v}_{1,j} - \mathbf{v}_{i,j}(z)\|_2^2, \quad (4)$$

where  $\mathbf{v}_{i,j}(z) \in \mathbb{R}^{3 \times q}$  stands for the re-parametrization in the  $i$ -th view, sampled using bilinear interpolation at a pixel position  $\mathbf{p}_{i,j}(z) \in \mathbb{R}^2$  calculated given the depth hypothesis  $z$ . This position is obtained by first back-projecting the reference patch pixel  $\mathbf{p}_{1,j} \in \mathcal{P}$  into 3D, and then projecting this 3D point into the control view:

$$\mathbf{p}_{i,j}(z) = \pi_i \circ \pi_z^{-1}(\mathbf{p}_{1,j}), \quad \forall \mathbf{p}_{1,j} \in \mathcal{P}, \quad (5)$$

where  $\pi_i$  denotes the projection from 3D world coordinates into the  $i$ -th control view’s image plane, and  $\pi_z^{-1}$  the inverse projection from a reference image pixel to its corresponding 3D point, given a depth hypothesis  $z$ .

To proceed with the actual optimization of (4), the function  $\pi_z^{-1}$  must now be made explicit, which typically involves a local geometric approximation (e.g., fronto-parallel or slanted patches). As we shall see next, the availability of normal information provides us with a natural way to avoid such an approximation.

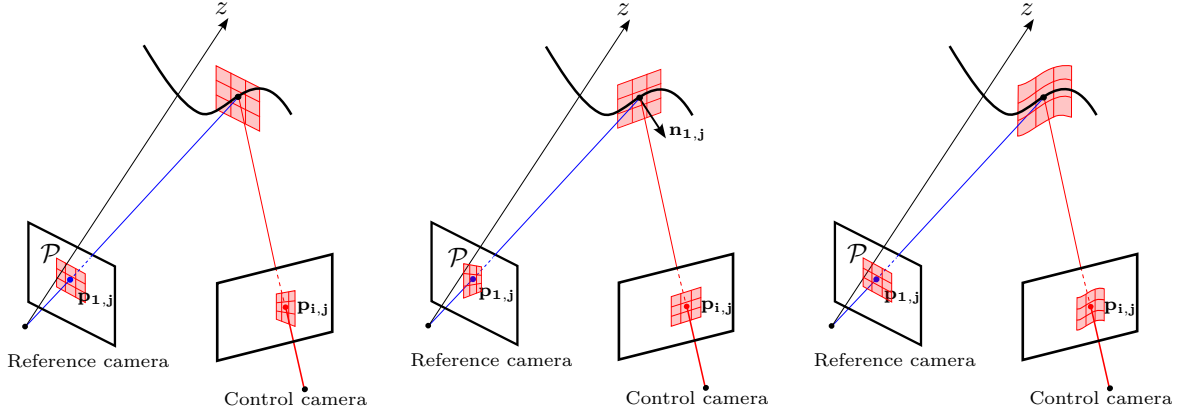


**Fig. 2:** The three types of patches. From left to right: fronto-parallel patches, slanted patches and (proposed) surface patches.

## 4.2 Exact Multi-view Integration

The most common approximations used in classical plane-sweeping MVS methods, which we illustrate in the first two diagrams of Figure 2, are:

- **Fronto-parallel patches** (zero-order approximation): all the patch points are assumed to lie on a plane parallel to the image plane, located at the hypothesized depth  $z$ . The inverse projection is then simply  $\pi_z^{-1}(\mathbf{p}_{1,j}) = z \mathbf{K}^{-1}[\mathbf{p}_{1,j}^\top \ 1]^\top$ , with  $\mathbf{K}$  the intrinsics matrix of the reference camera (assumed known a priori). This is the simplest model, but it is often inaccurate for non-planar surfaces or slanted views (Furukawa and Ponce, 2007; Furukawa et al, 2015).
- **Slanted patches** (first-order approximation): a finer approximation retains the depth  $z$  of the patch centre, yet assumes that the other points of the patch lie on a slanted plane, whose orientation is determined by the normal of the patch centre. Their depth is thus adjusted based on the plane equation (Bleyer et al, 2011; Schönberger et al, 2016; Calvet et al, 2023). This generally provides better accuracy than fronto-parallel patches, but approximation errors remain for curved surfaces.

In contrast, in our framework the detailed local geometry is fully encoded in the normal map  $\mathbf{N}_1$ , which allows us to move beyond simple planar approximations. Knowing the camera’s intrinsics, the normals  $\mathbf{n}_{1,j}$  in all pixels  $\mathbf{p}_{1,j} \in \mathcal{P}$  can indeed be integrated into depth values  $z \alpha_j$ , with  $\alpha_j = 1$  in the patch center. This means that the surface

patch is reconstructed up to a scale factor (Quéau et al, 2018), which is none other than the depth  $z$  of the patch centre. The inverse projection thus becomes:

$$\pi_z^{-1}(\mathbf{p}_{1,j}) = z \alpha_j \mathbf{K}^{-1}[\mathbf{p}_{1,j}^\top \ 1]^\top, \quad \forall \mathbf{p}_{1,j} \in \mathcal{P}, \quad (6)$$

Searching for the optimal  $z$  therefore amounts to achieve “surface sweeping”, without planar approximation.

By using this exact local surface representation, and the triangulation-based MVS framework (4) leveraging our re-parametrization, we not only enforce consistency in both appearance (reflectance) and detailed geometry (integrated normals) across views, but also avoid low-order approximation errors inherent to plane sweeping-based methods. This is empirically validated in the experiments presented hereafter.

## 4.3 Empirical Validation

To evaluate both the re-parametrization loss and the surface sweeping strategy, we generated a synthetic benchmark and compared our results against those obtained using traditional methods.

The **synthetic dataset** we created comprises two superimposed Gaussian functions, whose ground truth normals are computed analytically. The reflectance of the surface was set as a piecewise-linear function. We rendered  $N = 5$  normal and reflectance maps of this surface, using the camera parameters of the first five views of the Buddha dataset from DiLiGenT-MV (Li et al,

2020). Example normal and reflectance maps for two viewpoints are shown in Figure 3. This dataset allows us to evaluate surface reconstruction accuracy (in terms of mean depth error over the reference view) under known, ideal conditions (no noise, perfect normal/reflectance estimates) and to study the effect of controlled noise.

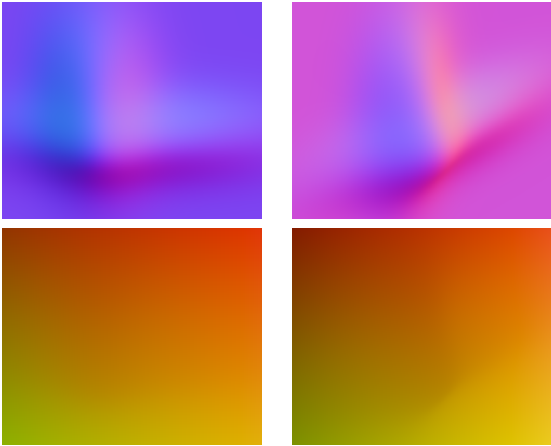


**Fig. 3:** Synthetic normals (top) and reflectance (bottom) used in our experiments, for the reference view (left) and one control view (right).

**Single-objective validation** is first considered, by comparing our results against a more straightforward solution combining a reflectance discrepancy loss  $\mathcal{L}_{\text{photo}}$  and a geometric one  $\mathcal{L}_{\text{geom}}$ , through a weighting hyperparameter  $\mu$ :

$$\min_{z>0} \sum_{i=2}^N \sum_{j=1}^{m_p} \left( \underbrace{(1 - \mathbf{n}_{1,j} \cdot \mathbf{n}_{i,j}(z))^2}_{\mathcal{L}_{\text{geom}}} + \mu \underbrace{\|\mathbf{r}_{1,j} - \mathbf{r}_{i,j}(z)\|_2^2}_{\mathcal{L}_{\text{photo}}} \right). \quad (7)$$

Therein, tuning  $\mu$  is often difficult, since its optimal value depends on the noise level. By unifying geometric and photometric cues into a single, parameter-free objective, the proposed re-parametrization circumvents this issue.

Figure 4 compares the mean depth error obtained using both approaches, in the presence of a fixed amount of additive Gaussian noise on the reflectance values (standard deviation: 1% of the maximum reflectance value) and an increasing one on the normals. To focus the evaluation on the re-parametrization, the same slanted patch approximation was adopted in both cases. While

the optimal value of  $\mu$  depends on the noise level, our hyperparameter-free approach always represents a reasonable compromise in performance, regardless of the noise level.

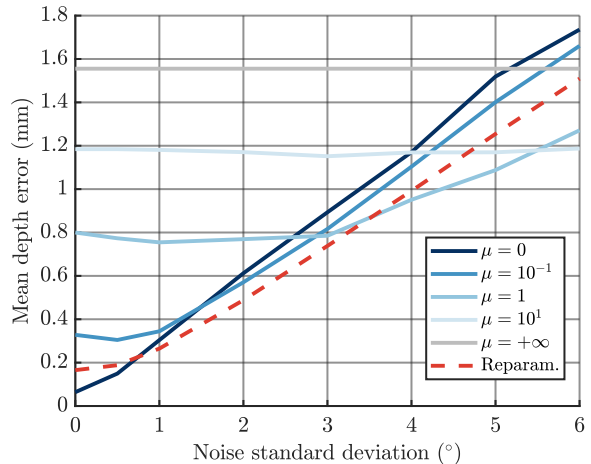


**Fig. 4:** Mean depth estimation error as a function of Gaussian noise added to input normal maps. The multi-objective approach is highly sensitive to the tuning of the hyperparameter  $\mu$ , while ours maintains stable results without such tuning.

**Surface sweeping validation** is then be assessed, by comparing the various patch geometry approximations. To focus only on the sweeping method, this time we considered only our single-objective loss, and noise was added only to normals, not reflectance. To also compare patch-based MVS methods against more modern frameworks, we included in the comparison our previous implementation of RNb-NeuS (Brument et al, 2024), based on volumetric rendering. The results are presented in Figure 5.

In the ideal, noiseless scenario, our proposed surface sweeping method leveraging normal integration achieves an essentially exact 3D reconstruction, demonstrating its capacity to eliminate the errors due to low-order patch geometry approximation. Such errors are indeed clearly visible on the first-order approximation (purple curve), and even more on the zero-order one (dark blue curve). The volumetric rendering approach (orange curve), on the other hand, presents a small, but non-null error, potentially stemming from inherent approximations within its neural

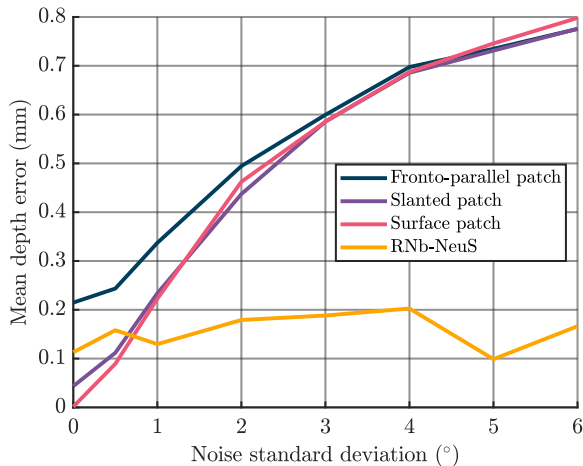


**Fig. 5:** Mean depth estimation error as a function of Gaussian noise added to input normals, for patch-based MVS method employing fronto-parallel plane sweeping (dark blue), slanted plane sweeping (purple), and normal-aware surface sweeping (pink), as well as the volumetric rendering method RNb-NeuS (Brument et al, 2024) (orange). Surface sweeping achieves exact reconstruction in the noiseless case, yet volumetric rendering is much more robust to high noise levels.

implicit representation and volume rendering process which may include local planarity assumptions (Wang et al, 2021b; Zhang et al, 2023b).

Adding noise to the normals reveals critical differences in robustness. The accuracy of all patch-based variants degrades as noise increases. Most notably, the surface sweeping approach, while perfect initially, rapidly deteriorates to the same level as lower-order approximations. This indicates that the accuracy of the local surface derived from normal integration is highly vulnerable to inaccuracies in the input normal field. On the other hand, volumetric rendering demonstrates considerably better robustness to high noise levels. This robustness likely benefits from its global optimization framework and the implicit regularization provided by the optimization of an SDF.

Overall, these empirical findings validate our hyperparameter-free re-parametrization strategy, and the feasibility of exact 3D reconstruction in ideal conditions. However, given that state-of-the-art photometric stereo methods often yield normals with mean angular errors in the range

$[5^\circ, 10^\circ]$  (Hardy et al, 2024), we believe that robustness to noise prevails over theoretical accuracy. Therefore, in the next section we turn our attention to coupling our re-parametrization with volumetric rendering frameworks.

## 5 Volume Rendering-based 3D Reconstruction

In contrast with the previous section where we focused on a single depth map, the present one introduces a method for estimating a full 3D model (geometry and reflectance) that is consistent with the input normal and reflectance data. To do so, we embed the homogeneous radiance-based re-parametrization introduced in Section 3 into a unified objective function derived from neural volume rendering (NVR) principles. The actual implementation builds upon the NeuS2 framework (Wang et al, 2023a), yielding a highly effective method for 3D reconstruction from multi-view normal and reflectance maps.

### 5.1 Surface Parametrization

We aim to infer a 3D model defined by two functions: a geometric map  $f : \mathbb{R}^3 \rightarrow \mathbb{R}$  and a photometric map  $\rho : \mathbb{R}^3 \rightarrow \mathbb{R}^q$ . Function  $f$  represents the signed distance to the surface, such that the surface  $\mathcal{S}$  is its zero-level set:  $\mathcal{S} = \{\mathbf{x} \in \mathbb{R}^3 \mid f(\mathbf{x}) = 0\}$ . Function  $\rho$  assigns a reflectance value to each 3D point. Since the actual form of  $\rho$  must be consistent with the assumptions from Section 3, we will limit ourselves to the Lambertian model ( $q = 1$ , or  $q = 3$  for RGB data), yet extensions to more complex BRDFs are conceivable as long as they are consistent with the PBR model used for re-parametrization.

### 5.2 Objective Function

For clarity within this subsection, we focus on data associated with a single camera view and omit the index  $i$ . Input reflectance and normal values are therefore denoted simply as  $\{\mathbf{r}_k\}_k$  and  $\{\mathbf{n}_k\}_k$ , and their joint re-parametrization as  $\{\mathbf{v}_k\}_k$ .

The core idea of our NVR approach is to optimize the scene representation  $(\rho, f)$  such that its rendering, under the same conditions as in Section 3, matches the input-derived radiance

vectors  $\mathbf{v}_k$ , by minimizing:

$$\mathcal{L}_{\text{NVR}}^p(\boldsymbol{\rho}, f) = \sum_{k=1}^m \|\tilde{\mathbf{v}}_k(\boldsymbol{\rho}, f) - \mathbf{v}_k\|_p^p, \quad (8)$$

with  $p \in \{1, 2\}$  (this choice will be discussed in the experiments), and where  $\tilde{\mathbf{v}}_k(\boldsymbol{\rho}, f)$  is the NVR-based radiance at pixel  $k$ .

The computation of the latter draws inspiration from NeuS (Wang et al, 2021b). Denoting  $\mathbf{o}$  the camera centre and  $\mathbf{d}_k$  the viewing direction associated with the  $k$ -th pixel, points along this ray write as  $\{\mathbf{x}_k(t) = \mathbf{o} + t\mathbf{d}_k \mid t \geq 0\}$ . Volume rendering then amounts to integrating individual colour contributions  $\mathbf{c}$  along this ray:

$$\tilde{\mathbf{v}}_k(\boldsymbol{\rho}, f) = \int_{t_0}^{t_1} w(t, f(\mathbf{x}_k(t))) \mathbf{c}(\mathbf{x}_k(t), \boldsymbol{\rho}, f) dt, \quad (9)$$

with  $[t_0, t_1]$  the integration range, and  $w$  an occlusion-aware weighting function ensuring concentration around the surface (Wang et al, 2021b).

Unlike the original NeuS which directly optimized apparent colour, we optimize the underlying surface properties by taking into account the PBR model  $F$  (it is crucial to use the same model as in (2)). Assimilating the unit outward surface normal to the gradient of the SDF, the apparent colour in (9) writes as:

$$\mathbf{c}(\mathbf{x}_k(t), \boldsymbol{\rho}, f) = F(\boldsymbol{\rho}(\mathbf{x}_k(t)), \nabla f(\mathbf{x}_k(t)), \mathbf{L}_k), \quad (10)$$

provided that  $\|\nabla f\| = 1$ . To simplify the optimization process, we followed NeuS and relaxed this hard constraint into an eikonal regularizer (encouraging  $\|\nabla f\|$  to be ‘‘close’’ to unity), controlled by some hyperparameter  $\lambda \geq 0$ :

$$\mathcal{L}_{\text{reg}}(f) = \lambda \frac{\sum_{k=1}^m \int_{t_0}^{t_1} (\|\nabla f(\mathbf{x}_k(t))\| - 1)^2 dt}{m(t_1 - t_0)}. \quad (11)$$

Combining (9) and (10) yields the NVR loss (8) for a single view. By averaging the contributions of all views, and adding the regularization (11) as well as the same silhouette consistency regularization as in NeuS (Wang et al, 2021b), we obtain our complete loss function. This formulation enables end-to-end optimization of the SDF  $f$  and reflectance  $\boldsymbol{\rho}$  using gradient-based methods, typically by representing  $f$  and  $\boldsymbol{\rho}$  as MLPs

and employing hierarchical sampling along rays, similar to NeuS (Wang et al, 2021b).

### 5.3 SuperNormal: A Specific Case

As stated in Section 3, in the absence of reflectance data, our framework can still be used, setting missing reflectance to constant white. If in addition, instead of the optimal triplet discussed in Section 3.3, one chooses a triplet of lights following the vectors of the canonical basis, then our framework actually comes down to a particular case which happens to be SuperNormal (Cao and Taketomi, 2024).

Indeed, using (2) and (3) with  $\mathbf{r}_{i,k} = [1]$  and  $\mathbf{L}_{i,k} = \mathbf{I}_3$ , the re-parametrized inputs simplify to the input normals:  $\mathbf{v}_{i,k} = \mathbf{n}_{i,k} \forall (i, k)$ . Similarly, using (9) and (10) with  $\boldsymbol{\rho} = \mathbf{1}$  and  $\mathbf{L}_k = \mathbf{I}_3$  yields the volumetric rendered normals:  $\tilde{\mathbf{n}}_k(f) := \int_{t_0}^{t_1} w(t, f(\mathbf{x}_k(t))) \nabla f(\mathbf{x}_k(t)) dt$ . With these two simplifications and  $p = 2$ , the NVR loss (8) becomes:

$$\mathcal{L}_{\text{SN}}(f) = \sum_{k=1}^m \|\tilde{\mathbf{n}}_k(f) - \mathbf{n}_k\|_2^2, \quad (12)$$

which is precisely the normal consistency loss introduced in SuperNormal. Upcoming experiments, presented in Section 6, will examine the performance obtained using this particular setting, in comparison with the proposed joint optimization over reflectance and normals using optimal triplets of light sources.

### 5.4 Reflectance Singularities

In comparison with SuperNormal, our approach has the advantage of taking into account not only normals, but also reflectance. However, this may sometimes turn into a drawback. Indeed, the actual reflectance values weight the optimization process, potentially leading to singularities e.g., in the presence of very dark materials. Let us demonstrate this under the Lambertian assumption, in the case of grey scale images ( $q = 1$ ). - For simplicity, let us consider an ideal sampling scenario where the weight  $w(\cdot, f(\mathbf{x}_k(\cdot)))$  in (9) is a Dirac function  $\delta_{t_k}(\cdot)$ , i.e. it is null everywhere except at some  $t_k$  such that  $\mathbf{x}_k := \mathbf{x}_k(t_k)$  lies on surface  $\mathcal{S}$ . By combining (3) and (10), the volumetric rendering (9) then simplifies to

$\tilde{\mathbf{v}}_k(\boldsymbol{\rho}, f) = \mathbf{L}_k \nabla f(\mathbf{x}_k) \boldsymbol{\rho}(\mathbf{x}_k)^\top$ . If  $q = 1$ , introducing the scalar variable  $R$  such that  $\boldsymbol{\rho}(\cdot) = \mathbf{r} R(\cdot)$ , the NVR loss (8) can be rewritten:

$$\mathcal{L}_{\text{NVR}}^p(R, f) = \sum_{k=1}^m |\mathbf{r}_k| \|R(\mathbf{x}_k) \mathbf{L}_k \nabla f(\mathbf{x}_k) - \mathbf{L}_k \mathbf{n}_k\|_p^p. \quad (13)$$

This rewriting emphasizes that reflectance acts as weighting factor in the loss function. Consequently, singular reflectance values may substantially influence the optimization of geometry. In particular, dark colours essentially leave the geometry locally unconstrained, which may result in slow, sub-optimal convergence and a loss of fine details (see Figure 6-(b)).

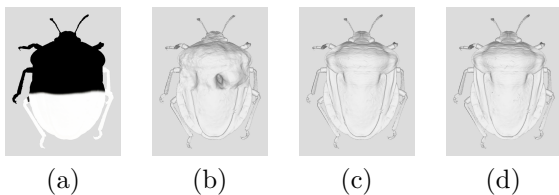


**Fig. 6:** Effect of reflectance embedding. (a) One of the input reflectance maps. (b) 3D reconstruction without reflectance embedding is deformed in the dark reflectance area. (c) With reflectance embedding, it is much closer to the ground truth (d).

To mitigate this issue, a reflectance embedding approach is introduced, which ensures that the reflectance norm remains constant. That is, we augment the input and estimated reflectance values as  $q + 1$ -dimensional vectors:

$$\mathbf{r}_k := \frac{1}{q} \left[ \mathbf{r}_k^\top, \left( q - \|\mathbf{r}_k\|_p^p \right)^{1/p} \right]^\top \quad \forall k, \quad (14)$$

$$\boldsymbol{\rho}(\cdot) := \frac{1}{q} \left[ \boldsymbol{\rho}(\cdot)^\top, \left( q - \|\boldsymbol{\rho}(\cdot)\|_p^p \right)^{1/p} \right]^\top. \quad (15)$$

It is easy to check that the norm of these vectors is equal to 1, whatever the values of  $p$  and  $q$ . This reflectance embedding strategy prevents any unintended influence of singular reflectance values on geometry optimization. This is qualitatively illustrated in Figure 6 on a synthetic experiment, using the  $L_1$ -norm ( $p = 1$ ) and grey level data ( $q = 1$ ). Therein, the dark regions are not faithfully reconstructed in the standard case, whereas reflectance

embedding significantly improves the results. Further experiments evaluating the interest of this embedding will be conducted in Section 6.

## 5.5 From RNb-NeuS to RNb-NeuS2

One of the main challenges with our initial approach, RNb-NeuS (Brument et al, 2024) built upon NeuS (Wang et al, 2021b), was the significant computation time required for a single reconstruction. The scene-dependent process indeed usually takes approximately 6-8 hours on a NVIDIA RTX 4090 GPU. To address this issue, we restructured our algorithm to follow the NeuS2 (Wang et al, 2023a) architecture. This results in a solution that is  $100\times$  faster, reducing computation time to around 5 minutes.

NeuS builds on NeRF (Mildenhall et al, 2021) by introducing volumetric rendering with a transfer function that converts an SDF into a density function. This allows direct optimization of scene geometry and extraction of a mesh via the SDF’s zero-level set. NeuS2 applies the same principles but replaces NeRF with Instant-NGP (Müller et al, 2022), which enables real-time rendering thanks to CUDA acceleration and the use of an optimizable hash grid for sampling during volumetric rendering. While CUDA contributes the most significant performance improvement, the hash grid further reduces computation time by focusing on surface-adjacent regions, enhancing detail preservation. NeuS2 retains these key optimizations while also including the SDF-based density representation from NeuS.

To transition RNb-NeuS to the NeuS2 framework, several modifications were required. The first one involved modifying the input structure to accommodate normal and albedo maps. Unlike NeuS, which predicts colour as a function of the viewing direction, RNb-NeuS estimates albedo, which is independent of the viewing direction. Consequently, this dependency had to be removed from the inputs of the albedo prediction network. With this adjustment, albedo could be retrieved at any point  $\mathbf{x}_k(t) \in \mathbb{R}^3$ , allowing colour prediction for each pixel following Equation (10).

The next phase involved implementing the necessary loss functions. While the eikonal loss (11) and the silhouette consistency one remained unchanged, adapting the colour loss was more

challenging. Indeed, the presence of a surface-aware PBR model in the colour prediction (10) fundamentally altered the gradient computations required for back-propagation. Unlike PyTorch, which supports automatic differentiation, NeuS2 is built entirely in CUDA, requiring manual specification of gradient computations. The details about the derivatives are in the supplementary material (Bruneau et al, 2025).

Now that we have outlined all the technical ingredients of the proposed method, let us present a series of experiments designed to evaluate its effectiveness across a range of scenarios.

## 6 Experimental Results

This section presents a thorough empirical evaluation of our approach. The multi-view multi-light scenario (MVPS) is first considered. Then, we carry out an ablation study over the individual components of our framework. Eventually, we demonstrate the use of our method in a multi-view single-light (MVS) setup. Thorough qualitative and quantitative results are provided in the supplementary material (Bruneau et al, 2025).

### 6.1 MVPS Materials

Our approach uses normal and reflectance maps, derivable from PS techniques. Multi-view multi-light datasets are thus key, as they enable independent PS per view, providing inputs for our integration process.

#### 6.1.1 Evaluation Datasets

**DiLiGenT-MV** (Li et al, 2020) is a benchmark of five real-world objects, some with complex reflectance and surface profiles. Each object is imaged from 20 calibrated viewpoints using the classical turntable MVPS acquisition setup (Hernández et al, 2008), under 96 directional lighting conditions. Given the acquisition characteristics, the relatively low image resolution of  $612 \times 512$  pixels corresponds to approximately 0.4 mm per pixel.

**LUCES-MV** (Logothetis et al, 2024) features 10 objects with a larger reflectance diversity than DiLiGenT-MV. Each object is captured from 12 different angles using a turntable setup, under 15 different near-light (non-directional) conditions.

Considering the low number of views and lighting conditions, LUCES-MV can be considered a “sparse” dataset. However, the image resolution ( $2080 \times 1552$  pixels) is significantly higher than that of DiLiGenT-MV. When related to the actual object size and the camera distance, this results in a finer scene resolution, where each pixel corresponds to approximately 0.13 mm.

**Skoltech3D** (Voynov et al, 2023) is a multi-sensor dataset designed for multi-view surface reconstruction. It includes 107 objects, among which we selected 20, focusing on the most challenging reflectance properties (transparency, specular, uniform texture). The acquisitions are performed under highly challenging lighting conditions (LED panels significantly deviating from the directional assumption), and often present over-exposed regions. For our evaluation, we used 20 views of the right camera, which is a TIS camera (*the imaging source*) of industrial type, and 12 illuminations per view. Although the image resolution is high ( $2368 \times 1952$ ), the increased object-to-camera distance results in a scene representation of approximately 0.3 mm per pixel, placing it between DiLiGenT-MV and LUCES-MV in terms of scene resolution.

#### 6.1.2 Photometric Stereo Methods

Given the variety of reflectance properties and illumination conditions in the selected MVPS datasets, state-of-the-art uncalibrated PS methods were selected, particularly transformers-based ones which exhibit strong performance even under unknown, general lighting conditions.

Among these methods, **SDM-UniPS** (Ikehata, 2023) (referred to as SDM in the result subsections) provides both normal and reflectance maps, enabling a complete evaluation of our pipeline. **UniMS-PS** (Hardy et al, 2024) predicts slightly more accurate normals (see Table 1), yet no reflectance. It thus allows only for normal integration assessment, similar to SuperNormal (Cao and Taketomi, 2024). To establish an upper bound on the achievable reconstruction quality, experiments were also conducted using ground truth normals. In the forthcoming experiments, the notation N: X (resp. N/R: X) indicates that the inputs are normals alone (resp. normals and reflectance), estimated with method X.

Since architecture constraints limit SDM-UniPS to use only 10 PS images, a sampling strategy was employed. Specifically, each  $\mathbf{r}_k$  and  $\mathbf{n}_k$  was computed as the median of the estimated reflectances and normals across 100 random trials, each trial involving 10 randomly chosen images. UniMS-PS scaling better thanks to multi-scale enhancement, sampling was not necessary.

		Normal MAE ( $^\circ$ ) $\downarrow$	
		SDM-UniPS	UniMS-PS
DiLiGenT-MV	Mean	6.79	5.17
	Std.	6.68	7.01
LUCES-MV	Mean	14.93	13.24
	Std.	11.36	10.22
Skoltech3D	Mean	17.25	18.51
	Std.	13.95	14.36

**Table 1:** Normal mean angular error for the two PS methods, on the three benchmarks. For each benchmark, ‘Mean’ indicates the averaged error on all datasets and ‘Std.’ its standard deviation.

The assessment of PS-estimated normals, conducted in Table 1, reveals that both methods exhibit a significant disparity across the datasets: while DiLiGenT-MV maintains an average MAE around  $6^\circ$ , LUCES-MV shows a much higher error ( $14^\circ$ ) and Skoltech3D an even higher one ( $18^\circ$ ). The input normals provided to our method can therefore be considered rather noisy.

### 6.1.3 Baselines

Our approach was compared against various MVPS techniques including, for DiLiGenT-MV, the classical methods Park16 (Park et al, 2016) and Li20 (Li et al, 2020), the neural approaches PS-NeRF (Yang et al, 2022), MVPSNet (Zhao et al, 2023), Kaya22 (Kaya et al, 2022) and Kaya23 (Kaya et al, 2023), and the most recent methods SuperNormal (Cao and Taketomi, 2024) and NPL-MVPS (Logothetis et al, 2025). Comparisons are more limited on LUCES-MV and Skoltech3D, as all methods were originally not benchmarked on these datasets, and are either proprietary or complex to reproduce.

Evaluations were also conducted against single-light MVS on DiLiGenT-MV. This required generating Lambertian-like images for each view, by computing for each viewpoint the median intensity across all lighting conditions, following

the approach of Li et al (2020) and Kaya et al (2022, 2023).

### 6.1.4 Metrics

To assess both the overall reconstruction and fine details, our quantitative evaluations rely on Chamfer distance (CD) and mean angular error (MAE). To highlight the ability to capture fine geometric details and the robustness in poorly constrained scenarios, we also provide a focus on clusters of particular interest – namely high curvature and low visibility areas, as illustrated in Figure 7. These clusters were segmented using VCGLib (Lab, 2011) and Meshlab (Cignoni et al, 2008), by retaining the vertices with maximal absolute principal curvature higher than 1.6 and those visible in less than 5 views, respectively.

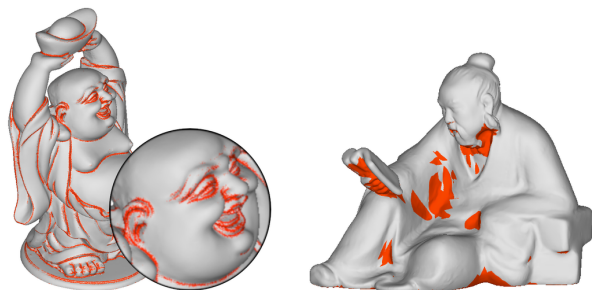


**Fig. 7:** High curvature (left) and low visibility (right) areas, on the Buddha and Reading datasets from DiLiGenT-MV.

## 6.2 MVPS Results

Unless otherwise specified, all subsequent evaluations are carried out using the  $\mathcal{L}_{\text{NVR}}^p$  loss with  $p = 2$ , an optimal lighting triplet and reflectance embedding, which has consistently shown the best performance across all evaluated datasets (see the ablation study in Section 6.3).

### 6.2.1 Results on DiLiGenT-MV

Table 2 presents the CD evaluation for the DiLiGenT-MV dataset. As a preliminary observation, let us remark the significant discrepancy (around  $-13\%$ ) between our results and those from the conference paper (RNb-NeuS), using the SDM-UniPS normal and reflectance maps. This

Chamfer distance (mm) ↓						
Methods	Bear	Buddha	Cow	Pot2	Reading	Mean
Park16	0.932	0.375	0.335	0.972	0.525	0.628
Li20 †	0.206	0.257	0.101	0.213	0.255	0.206
Kaya22	0.380	0.396	0.297	0.390	0.344	0.361
PS-NeRF	0.253	0.304	0.275	0.248	0.353	0.287
Kaya23	0.320	0.202	0.209	0.370	0.270	0.274
MVPSNet	0.288	0.272	0.244	0.296	0.243	0.269
SuperNormal (N: SDM)	0.177	0.206	0.186	0.141	0.222	0.186
NLP-MVPS	0.211	0.176	0.169	0.213	0.250	0.204
RNb-NeuS (N/R: SDM)	0.255	0.216	0.282	0.175	0.276	0.241
Ours (N/R: SDM)	0.218	0.222	0.180	0.143	0.284	0.209
Ours (N: SDM)	0.156	0.219	0.187	0.134	0.276	0.194
Ours (N: UniMS-PS)	0.157	0.183	0.154	0.148	0.191	0.167
Ours (N: GT)	0.127	0.069	0.097	0.083	0.090	0.093

**Table 2:** Chamfer distance (lower is better) averaged overall all vertices on DiLiGenT-MV dataset. Best results . Second best . Since † requires manual efforts (Li et al, 2020), it is not ranked.

Normal MAE (°) ↓						
Methods	Bear	Buddha	Cow	Pot2	Reading	Mean
Park16	14.39	14.09	12.06	16.25	17.02	14.76
Li20 †	4.16	10.76	2.99	5.87	11.68	7.09
Kaya22	6.44	14.11	5.87	9.91	12.42	9.75
PS-NeRF	4.82	10.88	5.62	6.72	13.75	8.36
Kaya23	3.88	7.41	3.29	6.32	10.90	6.36
MVPSNet	5.81	12.04	6.31	7.47	12.29	8.78
SuperNormal	3.12	7.14	3.30	4.28	10.88	5.75
NLP-MVPS	3.34	7.60	2.57	4.87	12.56	6.19
RNb-NeuS (N/R: SDM)	3.88	7.06	3.73	4.01	11.11	5.96
Ours (N/R: SDM)	3.07	7.87	3.48	4.22	11.46	6.02
Ours (N: SDM)	2.82	7.93	3.31	3.94	11.31	5.86
Ours (N: UniMS-PS)	2.66	7.39	3.09	3.97	10.00	5.42
Ours (N: GT)	2.10	2.40	1.89	1.79	6.86	3.01

**Table 3:** Normal MAE (lower is better) averaged over all views on the DiLiGenT-MV dataset.

discrepancy is due to the change of norm in the NVR loss (8), from  $p = 1$  to  $p = 2$ , which severely impacts the CD scores. As shown in the ablation study (Table 8), using the  $\mathcal{L}_{\text{NVR}}^1$  loss yields scores comparable with the conference paper.

Another notable observation is that whatever the PS method, our results are on par with state-of-the-art, or even better. Nevertheless, combining our method with UniMS-PS yields better results (−14%) than with SDM-UniPS, consistent with the higher accuracy of the former’s normals (see the first row of Table 1). This highlights the versatility of the proposed method, which adapts well to PS advancements.

On this dataset, reflectance seems not to really improve the results, yet its importance will become clearer later, when considering datasets exhibiting more challenging materials.

The conclusions of the MAE evaluation (Table 3) remain consistent with the CD one. A

last interesting observation is that using ground truth normals yields a non-null error, indicating a possible bias within the volumetric approach, as already noticed in Section 4.3.

Lastly, Figure 8 permits qualitative assessment of the overall reconstruction and its fine details.

### 6.2.2 Results on LUCES-MV

Experiments on LUCES-MV dataset (Table 4) confirmed our state-of-the-art results, yet here reflectance visibly improves the results. Interestingly, the CD scores largely increase in comparison with DiLiGenT-MV despite a better pixel resolution: for the Bowl object, even using GT normals, the CD is above 0.3 mm. We believe this could be due both to the sparser number of views — 12 vs 20 (Figure 9 indeed shows a strong correlation between CD and visibility) or to inaccuracies in the dataset’s camera calibration process.

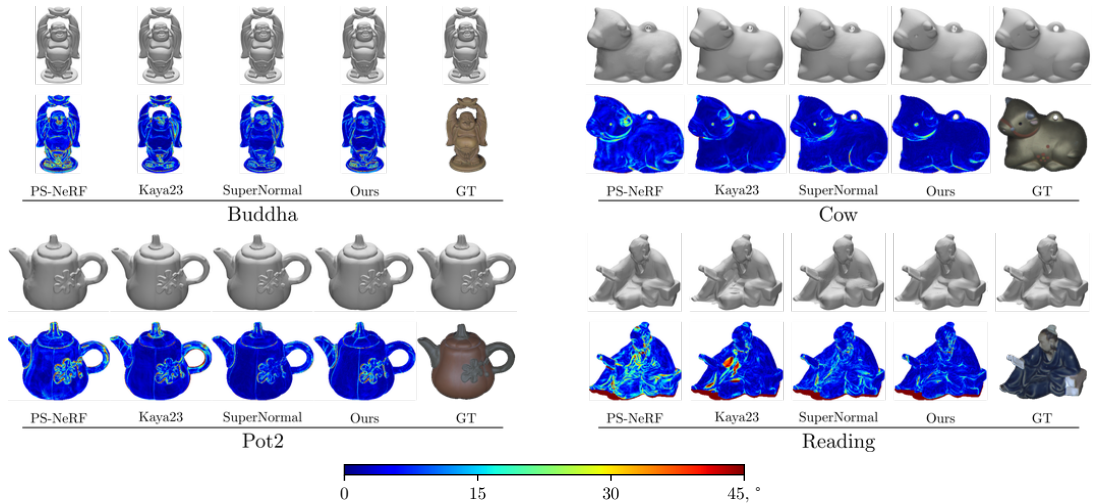


Fig. 8: Reconstructed 3D mesh and corresponding MAE of four objects from DiLiGenT-MV.

Chamfer distance (mm) ↓											
Methods	Bowl	Buddha	Bunny	Cup	Die	Hippo	House	Owl	Queen	Squirrel	Mean
SuperNormal (N: SDM)	0.832	0.828	0.274	0.770	0.408	0.421	0.836	0.586	0.342	0.301	0.560
Ours (N/R: SDM)	0.645	0.623	0.203	0.583	0.309	0.309	0.518	0.292	0.260	0.279	0.402
Ours (N: SDM)	0.624	0.757	0.230	0.609	0.339	0.335	0.542	0.321	0.273	0.276	0.431
Ours (N: UniMS-PS)	0.665	0.523	0.263	0.702	0.171	0.279	0.415	0.211	0.164	0.229	0.362
Ours (N: GT)	0.354	0.152	0.082	0.138	0.083	0.099	0.111	0.054	0.060	0.073	0.121

Table 4: Chamfer distance (lower is better) averaged overall all vertices on LUCES-MV.

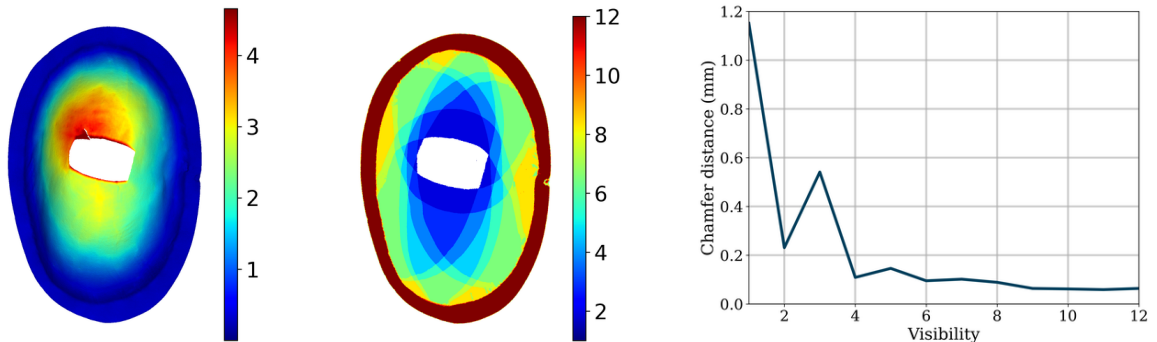


Fig. 9: Correlation between CD and visibility. From left to right: CD (in mm), number of cameras observing each vertex for LUCES-MV’s Bowl object, and CD vs visibility graph over the entire dataset.

### 6.2.3 Results on Skoltech3D

As for LUCES-MV, we compared our results on Skoltech3D against SuperNormal, which represents the state-of-the-art in MVPS. The CD reported in Table 5 emphasize the significant superiority of our results, as well as the interest of accounting for reflectance. Nevertheless, the

results on this dataset are globally disappointing, as can be seen in Figure 10 on two examples exhibiting severe breaks in the surface.

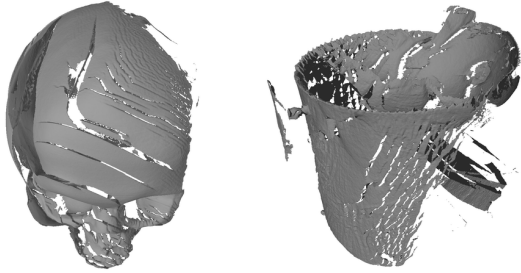
This is confirmed quantitatively by observing the strikingly high CD values. With similar spatial resolution and number of views as DiLiGenT-MV, the CD scores are drastically worse: the best-performing baseline’s CD (1.332 mm) being

Methods	dragon	golden_small	plush_bear	jin_chan	green_carved.	moon-pillow	paintcup	red_ceramic.	Painted_sam.	green_tea	blue_hoovings
NeuS2	1.012	0.462	0.582	0.710	1.187	0.236	1.123	0.246	1.332	0.997	1.557
SuperNormal (N: SDM)	1.334	0.959	1.225	0.762	2.360	2.678	1.939	2.806	2.196	2.201	1.585
Ours (N/R: SDM)	0.984	0.571	0.750	0.491	0.545	1.860	1.532	2.049	1.391	1.340	1.115
Ours (N: SDM)	1.034	0.630	0.920	0.461	0.602	2.381	1.710	2.510	1.714	1.694	1.288
Ours (N: UniMS-PS)	0.821	0.777	0.719	0.530	0.944	2.084	1.712	1.770	1.727	1.516	1.271
Ours (N: GT)	0.295	0.180	0.171	0.167	0.301	0.172	0.471	0.108	0.241	0.674	0.369

	golden_bust	small_wooden.	amber_vase	green_bucket	white_human.	orange_minni.	pink_boot	skate	white_castle.	wooden_trex	Mean
NeuS2	1.173	0.300	0.769	1.693	1.630	1.641	0.639	0.908	0.760	1.086	0.954
SuperNormal (N: SDM)	1.566	2.674	2.306	1.729	2.179	2.494	3.580	3.263	1.302	1.908	2.050
Ours (N/R: SDM)	0.772	1.562	0.872	2.175	1.667	2.134	1.592	2.450	1.071	1.040	1.332
Ours (N: SDM)	0.686	2.509	1.599	2.125	1.774	2.102	2.980	2.629	1.157	1.130	1.602
Ours (N: UniMS-PS)	0.751	1.702	1.525	2.396	1.655	1.902	3.207	2.716	0.815	0.906	1.497
Ours (N: GT)	0.218	0.127	0.244	1.640	0.269	0.197	0.441	0.430	0.289	0.360	0.351

**Table 5:** Chamfer distance (lower is better) averaged overall all vertices on Skoltech3D.



**Fig. 10:** Reconstruction of two objects from Skoltech3D. Clear surface ruptures can be observed.

around  $6\times$  higher than for DiLiGenT-MV (0.209 mm). This time, we believe that it is the quality of the PS normals (in over-saturated areas, notably) that is the bottleneck – as the very high PS errors from Table 1 tend to indicate.

A key indicator that this dataset is not suitable yet for multi-light studies is the comparison with NeuS2, chosen as single-light MVS baseline. NeuS2 achieves 27% better reconstructions than MVPS-based methods using 20 views. There is thus still room for improvement in PS/MVPS research, particularly in the presence of highly challenging illumination conditions.

## 6.2.4 High Curvature and Low Visibility Areas

As illustrated in Figure 11, the proposed method successfully reconstructs both low- and high-frequency geometric details. However, metrics averaged over the entire surface fail to report the accuracy in high curvature and low visibility areas. Therefore, targeted evaluations on these specific regions were conducted. The CD results on DiLiGenT-MV are reported in Table 6.

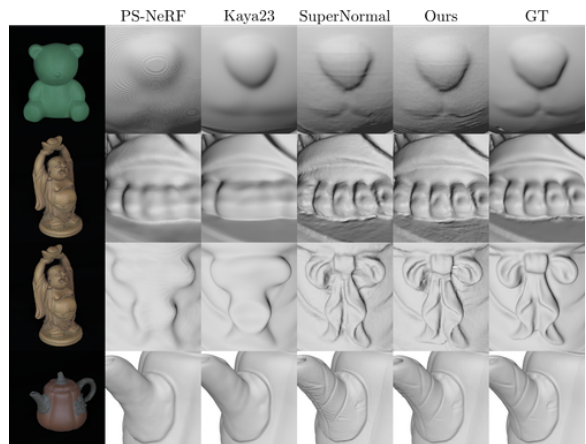


**Fig. 11:** Focus on the high-frequency details on the DiLiGenT-MV reconstructions.

	Chamfer distance (mm) ↓		
	All	High curv.	Diff.
% Vertices	100%	9.229%	
Park16	0.628	0.602	-0.026
Li20 †	0.206	0.572	+0.366
Kaya22	0.361	0.479	+0.118
PS-NeRF	0.287	0.439	+0.152
Kaya23	0.274	0.280	+0.006
MVPSNet	0.269	0.505	+0.236
SuperNormal (N: SDM)	0.186	0.215	+0.039
NPL-MVPS	0.204	0.258	+0.054
RNb-NeuS (N/R: SDM)	0.241	0.219	-0.022
Ours (N/R: SDM)	0.209	0.218	+0.009
Ours (N: SDM)	0.194	0.210	+0.016
Ours (N: UniMS-PS)	0.167	0.206	+0.039
Ours (N: GT)	0.093	0.079	-0.014
	All	Low vis.	Diff.
% Vertices	100%	9.494%	
Park16	0.628	0.707	+0.079
Li20 †	0.206	0.894	+0.688
Kaya22	0.361	0.610	+0.249
PS-NeRF	0.287	0.558	+0.271
Kaya23	0.274	0.363	+0.089
MVPSNet	0.269	0.571	+0.302
SuperNormal (N: SDM)	0.186	0.266	+0.080
NPL-MVPS	0.204	0.302	+0.098
RNb-NeuS (N/R: SDM)	0.241	0.286	+0.045
Ours (N/R: SDM)	0.209	0.266	+0.057
Ours (N: SDM)	0.194	0.273	+0.079
Ours (N: UniMS-PS)	0.167	0.240	+0.073
Ours (N: GT)	0.093	0.115	+0.022

**Table 6:** Chamfer distance on high curvature (top) and low visibility (bottom) areas, for the DiLiGenT-MV dataset.

The key insight from this table is found in the “difference” column, which compares the error for the entire point set against that of the selected subsets. As can be seen, the proposed method is significantly stabler than competitors on those challenging areas.

### 6.2.5 Sparse-View Scenario

One key advantage of using photometric stereo data is the richness of normal information. When these normals are of sufficiently high quality, as it is the case for the DiLiGenT-MV dataset, they impose strong constraints on the optimization process, enabling the proposed approach to perform well even in the sparse-view scenario, which is highly challenging for single-light MVS methods. This is assessed in Table 7, which reports the CD evolution when reducing the number of views from 20 to 5, for a panel of recent MVS methods and for the proposed one.

Methods	Chamfer distance (mm) ↓		
	20 views	10 views	5 views
NeuS	0.207	0.282	0.613
NeuS2	0.331	0.360	0.529
PET-NeuS	0.820	0.941	1.069
GaussianSurfels	0.973	1.080	0.894
RNb-NeuS (N/R: SDM)	0.241	0.229	0.269
Ours (N/R: SDM)	0.209	0.224	0.270
Ours (N: SDM)	0.194	0.218	0.260
Ours (N: UniMS-PS)	0.167	0.183	0.217
Ours (N: GT)	0.093	0.108	0.118

**Table 7:** Chamfer distance (lower is better) averaged overall all vertices on DiLiGenT-MV, for a decreasing number of views.

As expected, all MVS methods experience a significant drop in performance as the number of views decreases. In contrast, the proposed one remains much more stable in terms of CD. The primary effect of a reduced number of views for our method is a loss of fine details, as shown in Figure 12.

## 6.3 Ablations

Lastly, ablation studies were conducted on DiLiGenT-MV (Table 8) and LUCES-MV (Table 9) to quantify the impact of architectural choices within our method. More specifically, we compared the choice of  $p$  in the NVR loss  $\mathcal{L}_{\text{NVR}}^p$  (see Equation (8)), of considering reflectance maps ( $R$ ) in addition to normal maps, of using the pixel-wise optimal lighting triplets or the canonical ones ( $O$  vs  $C$ ), and of using reflectance embedding ( $+$ ) instead of a standard reflectance parametrization.

Lighting optimization appears important, yet to a less extent than the choice of  $p$ : using  $\mathcal{L}_{\text{NVR}}^2$  reduces CD scores by 9%. However,  $\mathcal{L}_{\text{NVR}}^1$  performs better when normals and reflectance are used together, while reflectance not always contributes positively using  $\mathcal{L}_{\text{NVR}}^2$ . Finally, reflectance embedding ( $+$ ) only slightly influences the metrics, which was to be expected since singular reflectance points are very sparse.

## 6.4 MVS Reconstruction

In addition to the MVPS use case, we also conducted a series of experiments in the single-light scenario. Therein, no reflectance input was fed to our method, and the normals were obtained using Colmap (Schönberger et al, 2016), which estimates

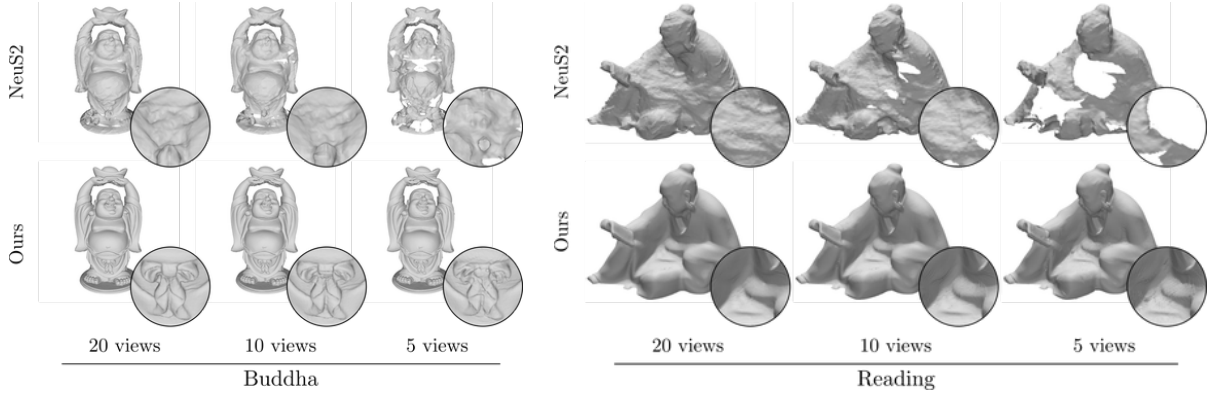


**Fig. 12:** Qualitative comparison between single-light NeuS2 and our method, in a sparse-view scenario on two objects from DiLiGenT-MV.

Chamfer distance (mm) ↓						
Methods	Bear	Buddha	Cow	Pot2	Reading	Mean
$\mathcal{L}^2\text{OR}+$	0.218	0.222	0.180	0.143	0.284	0.209
$\mathcal{L}^2\text{CR}+$	0.214	0.219	0.179	0.153	0.291	0.211
$\mathcal{L}^2\text{OR}$	0.219	0.230	0.176	0.174	0.304	0.221
$\mathcal{L}^2\text{O}$	0.156	0.219	0.187	0.134	0.276	0.194
$\mathcal{L}^1\text{OR}+$	0.212	0.232	0.255	0.136	0.305	0.228
$\mathcal{L}^1\text{CR}+$	0.196	0.235	0.271	0.164	0.291	0.231
$\mathcal{L}^1\text{OR}$	0.214	0.231	0.305	0.140	0.314	0.241
$\mathcal{L}^1\text{O}$	0.194	0.234	0.351	0.160	0.324	0.252

**Table 8:** Ablation study on DiLiGenT-MV, comparing the choice of  $p$  in the  $\mathcal{L}_{\text{NVR}}^p$  loss, the benefit of reflectance (R), optimal (O) or canonical (C) light triplets and finally that of reflectance embedding (+). For sake of clarity,  $\mathcal{L}_{\text{NVR}}^p$  is shown as  $\mathcal{L}^p$ .

them using PatchMatch (Bleyer et al, 2011). Additional tests were conducted using the single-view normal prediction method DSINE (Bae and Davison, 2024), however we did not include the results due to their significantly lower quality.

#### 6.4.1 Methodology

We compared our results against NeuS2 (Wang et al, 2023a) and Colmap (Schönberger et al, 2016), on 49 views of the same subset of 15 objects from DTU (Jensen et al, 2014) as in state-of-the-art methods.

Complementing the overall Chamfer distance, we employ a specific evaluation protocol to assess the reconstruction accuracy on fine geometric details, which can be averaged out by global metrics. Therefore, as previously we focus not only

on global reconstruction, but also on high curvature areas. However, the DTU objects being less “curvy” than other benchmarks, high curvature areas were segmented slightly differently, in order to focus on fine structures.

Ground truth points were first meshed using screened Poisson surface reconstruction, and this mesh was then smoothed via Laplacian filtering (Dawson-Haggerty et al., 2019). The displacement magnitude of each vertex during smoothing eventually served as a proxy for geometric frequency content, displacements above a hand-tuned threshold (1.5 mm) indicating fine structures. Figure 13 illustrates this segmentation approach.

#### 6.4.2 Results

The CD values on DTU are reported in Table 10. As can be observed, the proposed method is globally on par with alternative MVS frameworks.

However, our results are much stabler in the sparse-view scenario, as indicated in Table 11 where the number of views is decreased from 49 to 5. Our results are also much more accurate in high curvature areas, as indicated in these tables. Notably, although we use Colmap’s normals, our CDs are 10% lower in these areas, which highlights the interest of the proposed normal integration framework. Overall, these MVS experiments provide a proof of concept for the incorporation of our framework beyond MVPS.

Chamfer distance (mm) ↓											
Methods	Bowl	Buddha	Bunny	Cup	Die	Hippo	House	Owl	Queen	Squir.	Mean
$\mathcal{L}^2\text{OR}+$	0.645	0.623	0.203	0.583	0.309	0.309	0.518	0.292	0.260	0.279	0.402
$\mathcal{L}^2\text{CR}+$	0.630	0.595	0.226	0.563	0.356	0.376	0.540	0.312	0.336	0.365	0.430
$\mathcal{L}^2\text{OR}$	0.642	0.628	0.190	0.570	0.336	0.310	0.514	0.246	0.337	0.314	0.409
$\mathcal{L}^2\text{O}$	0.624	0.757	0.230	0.609	0.339	0.335	0.542	0.321	0.273	0.276	0.431
$\mathcal{L}^1\text{OR}+$	0.764	0.834	0.264	0.757	0.295	0.384	0.524	0.333	0.308	0.287	0.475
$\mathcal{L}^1\text{CR}+$	0.801	0.891	0.266	0.758	0.303	0.387	0.581	0.420	0.368	0.298	0.507
$\mathcal{L}^1\text{OR}$	0.762	0.813	0.235	0.682	0.263	0.356	0.489	0.316	0.295	0.286	0.450
$\mathcal{L}^1\text{O}$	0.873	0.899	0.332	0.746	0.434	0.437	0.580	0.415	0.367	0.317	0.540

**Table 9:** Ablation study on LUCES-MV, with the same notations as in Table 8.

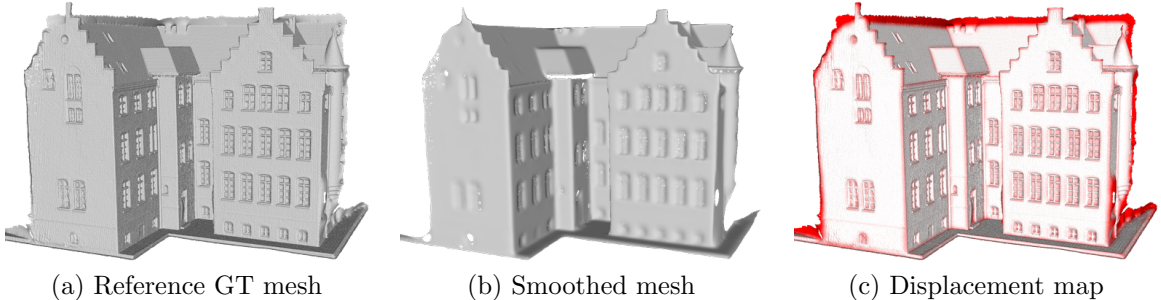


**Fig. 13:** High curvature segmentation for the scan24 object of DTU. The ground truth mesh (a), obtained via Poisson reconstruction, is smoothed using the Laplacian operator (b). The displacement magnitude (c) is then thresholded to identify the finest structures.

## 7 Conclusion and Perspectives

We presented a versatile and efficient framework for high-fidelity 3D surface reconstruction by leveraging multi-view normal cues, with optional use of reflectance information. Through a novel reparametrization of normals and reflectance as radiance vectors simulated under varying illumination, our method fits seamlessly into both traditional MVS and NVR pipelines. It is also very fast, thanks to CUDA acceleration and an optimizable hash grid. Extensive experiments on the most recent benchmarks demonstrate state-of-the-art performance, particularly in capturing fine details and handling challenging reflectance and visibility conditions.

However, challenges remain. We observe bias in the volume rendering version when using ground truth normals, and robustness to noisy input normals still needs improvement. These limitations underline the importance of better PS estimation, especially with a limited number of light sources.

Moreover, our findings suggest the need for more reliable MVPS datasets. Notably, reconstruction accuracy paradoxically decreases with increasing image resolution on current benchmarks (see for example results on DiLiGenT-MV and LUCES-MV), an observation that questions the ground truth quality of recent datasets.

More broadly, this work highlights the practical promise of MVPS over traditional MVS and single-light methods. With recent PS techniques (e.g., SDM-UniPS, UniMS-PS) delivering accurate normals under complex reflectance, and with multi-view normal integration methods (e.g., SuperNormal, ours) preserving fine details, MVPS emerges as a compelling option for accurate, affordable 3D scanning – especially in semi-controlled environments. It also significantly outperforms single-illumination methods on objects with deep concavities (see Figure 14) or transparent parts (see Figure 15), by leveraging the rich geometric cues offered by multi-light and ViT-based priors.

Chamfer distance (mm) ↓								
All								
Methods	24	37	40	55	63	65	69	83
Colmap	0.41	0.85	0.37	0.37	0.88	1.00	0.52	1.17
NeuS2	0.92	0.72	1.28	0.30	0.99	0.88	0.62	1.36
Ours $\mathcal{L}^1$ (N: Schönberger et al (2016))	0.36	0.95	0.38	0.28	0.90	0.91	0.63	1.27
Ours $\mathcal{L}^2$ (N: Schönberger et al (2016))	0.41	1.23	0.36	0.37	0.95	1.04	0.73	1.30
	97	105	106	110	114	118	122	Mean
	1.09	0.61	0.52	0.50	0.31	0.42	0.42	0.63
	1.62	0.82	0.58	0.80	0.37	0.40	0.39	0.80
	1.33	0.71	0.49	0.53	0.34	0.44	0.42	0.66
	1.49	0.70	0.53	0.59	0.48	0.49	0.48	0.74
High curvatures								
Methods	24	37	40	55	63	65	69	83
Colmap	1.18	2.33	1.56	2.37	3.84	3.14	1.98	2.96
NeuS2	1.38	2.01	2.80	1.18	3.45	3.15	1.69	3.14
Ours $\mathcal{L}^1$ (N: Schönberger et al (2016))	0.88	2.43	1.41	1.18	3.10	2.50	1.61	2.86
Ours $\mathcal{L}^2$ (N: Schönberger et al (2016))	0.96	2.17	1.38	1.33	2.65	2.62	1.68	2.87
	97	105	106	110	114	118	122	Mean
	2.46	2.05	2.08	1.88	0.91	1.58	1.27	2.21
	3.31	2.28	1.35	2.40	1.01	1.43	1.16	2.17
	1.88	1.93	1.52	1.90	1.08	1.52	1.27	1.90
	1.88	2.04	1.86	1.85	1.49	1.64	1.36	1.90

**Table 10:** Chamfer distance on 15 objects of DTU, globally (top) and for high curvature areas only (bottom). For sake of clarity,  $\mathcal{L}_{\text{NVR}}^p$  is shown as  $\mathcal{L}^p$ .

Chamfer distance (mm) ↓					
All					
Methods	49 views	30 views	20 views	10 views	5 views
Colmap	0.63	0.63	0.66	1.14	2.11
NeuS2	0.80	0.85	1.43	2.53	2.05
Ours $\mathcal{L}^1$ (N: Schönberger et al (2016))	0.66	0.70	1.15	1.73	1.77
Ours $\mathcal{L}^2$ (N: Schönberger et al (2016))	0.74	0.79	1.22	1.61	1.83
High curvatures					
Methods	49 views	30 views	20 views	10 views	5 views
Colmap	2.21	2.37	2.66	3.35	4.49
NeuS2	2.17	2.26	2.45	2.93	4.03
Ours $\mathcal{L}^1$ (N: Schönberger et al (2016))	1.90	1.97	2.10	2.72	3.70
Ours $\mathcal{L}^2$ (N: Schönberger et al (2016))	1.90	1.94	2.10	2.72	3.47

**Table 11:** Chamfer distance on DTU averaged overall all vertices (top) and high curvature areas (bottom), for a decreasing number of views. For sake of clarity,  $\mathcal{L}_{\text{NVR}}^p$  is shown as  $\mathcal{L}^p$ .

We hope this work encourages further exploration of this paradigm, from improving robustness and dataset quality to enabling broader applicability in real-world scenarios.

## Funding

Robin Bruneau’s postdoctoral fellowship was funded by the Department of Quantitative Biomedicine at the University of Zurich. Baptiste Brument’s doctoral student fellowship was

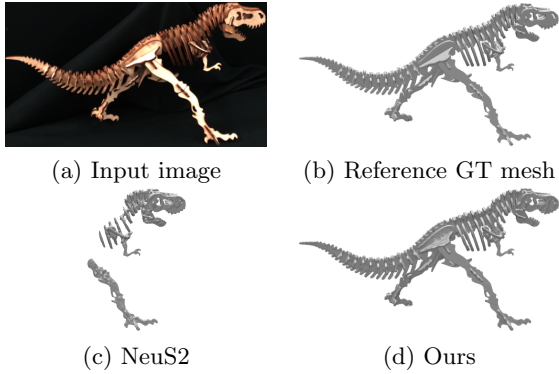


**Fig. 14:** Advantage of MVPS (d) over MVS (c) beyond fine detail reconstruction: handling deep concavities (`wooden_trex` from the Skoltech3D dataset) associated to low visibility areas.

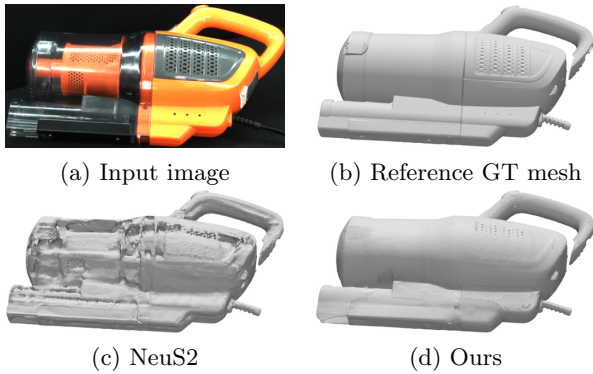


**Fig. 15:** Advantage of MVPS (d) over MVS (c) beyond fine detail reconstruction: handling transparency (`orange_mini_vacuum` from the Skoltech3D dataset; see transparent cover). This is enabled by the high diversity of light reflections, which are effectively leveraged by recent PS techniques.

funded by the CNRS through the project OpenDOPAMIn. Lilian Calvet’s postdoctoral fellowship was supported by the University of Zurich, the University Hospital of Balgrist, and the OR-X - a Swiss national research infrastructure for translational surgery. The research leading to these results received funding from the French National Research Agency (ANR) through the LabCom project ALICIA-Vision, and by the Department of Computer Science at the University of Copenhagen (DIKU) through the Copenhagen Data+ project PHYLORAMA.

## Data Availability

The code and data relative to this article are available at <https://github.com/RobinBruneau/RNb-NeuS2>. Also, a thorough qualitative and quantitative study is available in the supplementary material (Bruneau et al, 2025) at [https://drive.google.com/file/d/1KdfCKediXNP5Os954TL\\_QldaUWS0nKcD/view?usp=drive\\_link](https://drive.google.com/file/d/1KdfCKediXNP5Os954TL_QldaUWS0nKcD/view?usp=drive_link).

The DiLiGenT-MV dataset (Li et al, 2020) is available at <https://sites.google.com/site/photometricstereodata/mv>. The LUCES-MV dataset (Logothetis et al, 2024) is available at <https://drive.google.com/drive/folders/1634yweYUpLvNPC1qEG8hRpmhtxVtFrLi?usp=sharing>. The Skoltech3D dataset (Voynov et al, 2023) is available at <https://skoltech3d.appliedai.tech/>.

## References

- Alldrin NG, Mallick SP, Kriegman DJ (2007) Resolving the generalized bas-relief ambiguity by entropy minimization. In: Proceedings of the IEEE Conference on Computer Vision and Pattern Recognition, pp 1–7
- Bae G, Davison AJ (2024) Rethinking Inductive Biases for Surface Normal Estimation. In: Proceedings of the IEEE/CVF Conference on Computer Vision and Pattern Recognition
- Bae G, Budvytis I, Cipolla R (2021) Estimating and exploiting the aleatoric uncertainty in surface normal estimation. In: Proceedings of the 18th IEEE/CVF International Conference on Computer Vision, pp 13137–13146
- Bae G, Budvytis I, Cipolla R (2022) IronDepth: Iterative Refinement of Single-View Depth using Surface Normal and its Uncertainty. In: Proceedings of the 33rd British Machine Vision Conference
- Basri R, Jacobs D, Kemelmacher I (2007) Photometric stereo with general, unknown lighting. *International Journal of Computer Vision* 72:239–257
- Bleyer M, Rhemann C, Rother C (2011) Patch-match stereo-stereo matching with slanted support windows. In: Proceedings of the 22nd British Machine Vision Conference, pp 1–11
- Brument B, Bruneau R, Quéau Y, et al (2024) RNb-NeuS: Reflectance and Normal-based Multi-View 3D Reconstruction. In: Proceedings of the IEEE/CVF Conference on Computer Vision and Pattern Recognition
- Bruneau R, Brument B, Quéau Y, et al (2025) Multi-view Surface Reconstruction Using Normal and Reflectance Cues - Supplementary Material. [https://drive.google.com/file/d/1KDfCKediXNP5Os954TL.QldaUWS0nKcD/view?usp=drive\\_link](https://drive.google.com/file/d/1KDfCKediXNP5Os954TL.QldaUWS0nKcD/view?usp=drive_link)
- Calvet L, Maignan N, Brument B, et al (2023) Multi-view Normal Estimation – Application to Slanted Plane-Sweeping. In: Proceedings of the 9th International Conference on Scale Space and Variational Methods in Computer Vision, pp 704–716
- Cao X, Taketomi T (2024) SuperNormal: Neural Surface Reconstruction via Multi-View Normal Integration. In: Proceedings of the IEEE/CVF Conference on Computer Vision and Pattern Recognition, pp 20581–20590
- Chandraker MK, Kahl F, Kriegman DJ (2005) Reflections on the generalized bas-relief ambiguity. In: Proceedings of the IEEE Conference on Computer Vision and Pattern Recognition, pp 788–795
- Chen G, Han K, Wong KYK (2018) PS-FCN: A flexible learning framework for photometric stereo. In: Proceedings of the 15th European Conference on Computer Vision, pp 3–18
- Chen G, Han K, Shi B, et al (2019) Self-calibrating deep photometric stereo networks. In: Proceedings of the IEEE/CVF Conference on Computer Vision and Pattern Recognition, pp 8739–8747
- Chen G, Waechter M, Shi B, et al (2020) What is learned in deep uncalibrated photometric stereo? In: Proceedings of the 16th European Conference on Computer Vision, pp 745–762
- Cignoni P, Callieri M, Corsini M, et al (2008) Meshlab: an open-source mesh processing tool. In: Proceedings of the Eurographics Italian Chapter Conference, pp 129–136
- Collins RT (1996) A space-sweep approach to true multi-image matching. In: Proceedings of the IEEE Conference on Computer Vision and Pattern Recognition, pp 358–363
- Dai P, Xu J, Xie W, et al (2024) High-quality surface reconstruction using gaussian surfels. In: ACM SIGGRAPH 2024 Conference Papers, pp 1–11
- Dawson-Haggerty et al. (2019) trimesh. URL <https://trimesh.org/>
- Do T, Vuong K, Roumeliotis SI, et al (2020) Surface normal estimation of tilted images via spatial rectifier. In: Proceedings of the 16th European Conference on Computer Vision, pp

- Drbohlav O, Chantler M (2005) On optimal light configurations in photometric stereo. In: Proceedings of the 10th IEEE International Conference on Computer Vision, pp 1707–1712
- Eftekhari A, Sax A, Malik J, et al (2021) Omnidata: A Scalable Pipeline for Making Multi-Task Mid-Level Vision Datasets From 3D Scans. In: Proceedings of the 18th IEEE/CVF International Conference on Computer Vision, pp 10786–10796
- Eigen D, Fergus R (2015) Predicting depth, surface normals and semantic labels with a common multi-scale convolutional architecture. In: Proceedings of the 15th IEEE International Conference on Computer Vision, pp 2650–2658
- Engelhardt A, Raj A, Boss M, et al (2024) SHINOBI: Shape and Illumination using Neural Object Decomposition via BRDF Optimization In-the-wild. In: Proceedings of the IEEE/CVF Conference on Computer Vision and Pattern Recognition
- Favaro P, Papadimitriou T (2012) A closed-form solution to uncalibrated photometric stereo via diffuse maxima. In: Proceedings of the IEEE Conference on Computer Vision and Pattern Recognition, pp 821–828
- Furukawa Y, Ponce J (2007) Accurate, dense, and robust multi-view stereopsis. In: Proceedings of the IEEE Conference on Computer Vision and Pattern Recognition
- Furukawa Y, Hernández C, et al (2015) Multi-view stereo: A tutorial. *Foundations and Trends in Computer Graphics and Vision* 9(1-2):1–148
- Goldman DB, Curless B, Hertzmann A, et al (2009) Shape and spatially-varying brdfs from photometric stereo. *IEEE Transactions on Pattern Analysis and Machine Intelligence* 32(6):1060–1071
- Gu X, Fan Z, Zhu S, et al (2020) Cascade cost volume for high-resolution multi-view stereo and stereo matching. In: Proceedings of the IEEE/CVF Conference on Computer Vision and Pattern Recognition, pp 2495–2504
- Guo H, Mo Z, Shi B, et al (2021) Patch-based uncalibrated photometric stereo under natural illumination. *IEEE Transactions on Pattern Analysis and Machine Intelligence* 44(11):7809–7823
- Haefner B, Ye Z, Gao M, et al (2019) Variational uncalibrated photometric stereo under general lighting. In: Proceedings of the 17th IEEE/CVF International Conference on Computer Vision, pp 8539–8548
- Hardy C, Quéau Y, Tschumperlé D (2024) Uni MS-PS: A multi-scale encoder-decoder transformer for universal photometric stereo. *Computer Vision and Image Understanding* 248:104093
- Hayakawa H (1994) Photometric stereo under a light source with arbitrary motion. *Journal of the Optical Society of America A* 11(11):3079–3089
- Hernández C, Vogiatzis G, Cipolla R (2008) Multiview Photometric Stereo. *IEEE Transactions on Pattern Analysis and Machine Intelligence* 30(3):548–554
- Ikehata S (2018) CNN-PS: CNN-based photometric stereo for general non-convex surfaces. In: Proceedings of the 15th European Conference on Computer Vision, pp 3–18
- Ikehata S (2022a) Ps-transformer: Learning sparse photometric stereo network using self-attention mechanism. In: Proceedings of the 33rd British Machine Vision Conference
- Ikehata S (2022b) Universal photometric stereo network using global lighting contexts. In: Proceedings of the IEEE/CVF Conference on Computer Vision and Pattern Recognition, pp 12591–12600
- Ikehata S (2023) Scalable, Detailed and Mask-Free Universal Photometric Stereo. In: Proceedings of the IEEE/CVF Conference on Computer Vision and Pattern Recognition, pp 13198–13207

- Ikehata S, Aizawa K (2014) Photometric stereo using constrained bivariate regression for general isotropic surfaces. In: Proceedings of the IEEE Conference on Computer Vision and Pattern Recognition, pp 2179–2186
- Ikehata S, Wipf D, Matsushita Y, et al (2012) Robust photometric stereo using sparse regression. In: Proceedings of the IEEE Conference on Computer Vision and Pattern Recognition, pp 318–325
- Jensen R, Dahl A, Vogiatzis G, et al (2014) Large scale multi-view stereopsis evaluation. In: Proceedings of the IEEE Conference on Computer Vision and Pattern Recognition, pp 406–413
- Ju Y, Shi B, Wen B, et al (2025) Revisiting One-stage Deep Uncalibrated Photometric Stereo via Fourier Embedding. *IEEE Transactions on Pattern Analysis and Machine Intelligence*
- Kar OF, Yeo T, Atanov A, et al (2022) 3D Common Corruptions and Data Augmentation. In: Proceedings of the IEEE/CVF Conference on Computer Vision and Pattern Recognition, pp 18963–18974
- Kaya B, Kumar S, Oliveira C, et al (2021) Uncalibrated neural inverse rendering for photometric stereo of general surfaces. In: Proceedings of the IEEE/CVF Conference on Computer Vision and Pattern Recognition, pp 3804–3814
- Kaya B, Kumar S, Oliveira C, et al (2022) Uncertainty-aware deep multi-view photometric stereo. In: Proceedings of the IEEE/CVF Conference on Computer Vision and Pattern Recognition, pp 12601–12611
- Kaya B, Kumar S, Oliveira C, et al (2023) Multi-View Photometric Stereo Revisited. In: Proceedings of the IEEE/CVF Winter Conference on Applications of Computer Vision, pp 3126–3135
- Kerbl B, Kopanas G, Leimkühler T, et al (2023) 3D Gaussian Splatting for Real-Time Radiance Field Rendering. *ACM Transactions on Graphics* 42(4)
- Kolesnikov A, Dosovitskiy A, Weissenborn D, et al (2021) An Image is Worth 16x16 Words: Transformers for Image Recognition at Scale. In: Proceedings of the 9th International Conference on Learning Representations
- Lab VC (2011) A portable C++ templated library for the manipulation, processing of triangle and tetrahedral meshes
- Li B, Shen C, Dai Y, et al (2015) Depth and surface normal estimation from monocular images using regression on deep features and hierarchical crfs. In: Proceedings of the IEEE Conference on Computer Vision and Pattern Recognition, pp 1119–1127
- Li J, Li H (2022) Self-calibrating photometric stereo by neural inverse rendering. In: Proceedings of the 17th European Conference on Computer Vision, pp 166–183
- Li M, Zhou Z, Wu Z, et al (2020) Multi-view photometric stereo: A robust solution and benchmark dataset for spatially varying isotropic materials. *IEEE Transactions on Image Processing* 29:4159–4173
- Li Z, Müller T, Evans A, et al (2023) Neuralangelo: High-Fidelity Neural Surface Reconstruction. In: Proceedings of the IEEE/CVF Conference on Computer Vision and Pattern Recognition, pp 8456–8465
- Liang R, Gojcic Z, Ling H, et al (2025) DiffusionRenderer: Neural Inverse and Forward Rendering with Video Diffusion Models. In: Proceedings of the IEEE/CVF Conference on Computer Vision and Pattern Recognition
- Liao S, Gavves E, Snoek CG (2019) Spherical regression: Learning viewpoints, surface normals and 3D rotations on n-spheres. In: Proceedings of the IEEE/CVF Conference on Computer Vision and Pattern Recognition, pp 9759–9767
- Logothetis F, Mecca R, Cipolla R (2019) A differential volumetric approach to multi-view photometric stereo. In: Proceedings of the 17th IEEE/CVF International Conference on Computer Vision, pp 1052–1061

- Logothetis F, Budvytis I, Liwicki S, et al (2024) LUCES-MV: A Multi-View Dataset for Near-Field Point Light Source Photometric Stereo. arXiv preprint arXiv:241216737
- Logothetis F, Budvytis I, Cipolla R (2025) NPL-MVPS: Neural Point-Light Multi-View Photometric Stereo. In: Proceedings of the IEEE/CVF Winter Conference on Applications of Computer Vision, pp 2291–2300
- Long X, Zheng Y, Zheng Y, et al (2024) Adaptive surface normal constraint for geometric estimation from monocular images. IEEE Transactions on Pattern Analysis and Machine Intelligence
- Lopes I, Pizzati F, de Charette R (2024) Material Palette: Extraction of Materials from a Single Image. In: Proceedings of the IEEE/CVF Conference on Computer Vision and Pattern Recognition
- Mildenhall B, Srinivasan PP, Tancik M, et al (2021) NeRF: Representing Scenes as Neural Radiance Fields for View Synthesis. Communications of the ACM 65(1):99–106
- Mo Z, Shi B, Lu F, et al (2018) Uncalibrated photometric stereo under natural illumination. In: Proceedings of the IEEE/CVF Conference on Computer Vision and Pattern Recognition, pp 2936–2945
- Müller T, Evans A, Schied C, et al (2022) Instant Neural Graphics Primitives with a Multiresolution Hash Encoding. ACM Transactions on Graphics 41(4)
- Nehab D, Rusinkiewicz S, Davis J, et al (2005) Efficiently combining positions and normals for precise 3D geometry. ACM Transactions on Graphics 24(3):536–543
- Oechsle M, Peng S, Geiger A (2021) Unisurf: Unifying neural implicit surfaces and radiance fields for multi-view reconstruction. In: Proceedings of the 18th IEEE/CVF International Conference on Computer Vision, pp 5589–5599
- Park J, Sinha SN, Matsushita Y, et al (2013) Multiview photometric stereo using planar mesh parameterization. In: Proceedings of the 14th IEEE International Conference on Computer Vision, pp 1161–1168
- Park J, Sinha SN, Matsushita Y, et al (2016) Robust multiview photometric stereo using planar mesh parameterization. IEEE Transactions on Pattern Analysis and Machine Intelligence 39(8):1591–1604
- Qi X, Liao R, Liu Z, et al (2018) Geonet: Geometric neural network for joint depth and surface normal estimation. In: Proceedings of the IEEE Conference on Computer Vision and Pattern Recognition, pp 283–291
- Qi X, Liu Z, Liao R, et al (2020) Geonet++: Iterative geometric neural network with edge-aware refinement for joint depth and surface normal estimation. IEEE Transactions on Pattern Analysis and Machine Intelligence 44(2):969–984
- Quéau Y, Lauze F, Durou JD (2015) A L1-TV Algorithm for Robust Perspective Photometric Stereo with Spatially-Varying Lightings. In: Proceedings of the 5th International Conference on Scale Space and Variational Methods in Computer Vision, pp 498–510
- Quéau Y, Wu T, Durou JD, et al (2017) A Non-Convex Variational Approach to Photometric Stereo under Inaccurate Lighting. In: Proceedings of the IEEE Conference on Computer Vision and Pattern Recognition, pp 99–108
- Quéau Y, Durou JD, Aujol JF (2018) Normal integration: A survey. Journal of Mathematical Imaging and Vision 60:576–593
- Santo H, Samejima M, Sugano Y, et al (2017) Deep photometric stereo network. In: Proceedings of the 16th IEEE International Conference on Computer Vision Workshops, pp 501–509
- Schönberger JL, Zheng E, Frahm JM, et al (2016) Pixelwise view selection for unstructured multi-view stereo. In: Proceedings of the 14th European Conference on Computer Vision, pp 501–518
- Seitz SM, Curless B, Diebel J, et al (2006) A comparison and evaluation of multi-view stereo

- reconstruction algorithms. In: Proceedings of the IEEE Conference on Computer Vision and Pattern Recognition, pp 519–528
- Shi B, Tan P, Matsushita Y, et al (2012) A biquadratic reflectance model for radiometric image analysis. In: Proceedings of the IEEE Conference on Computer Vision and Pattern Recognition, pp 230–237
- Silberman N, Hoiem D, Kohli P, et al (2012) Indoor segmentation and support inference from rgb-d images. In: Proceedings of the 12th European Conference on Computer Vision, pp 746–760
- Taniai T, Maehara T (2018) Neural inverse rendering for general reflectance photometric stereo. In: Proceedings of the 35th International Conference on Machine Learning, pp 4857–4866
- Verbin D, Hedman P, Mildenhall B, et al (2022) Ref-NeRF: Structured View-Dependent Appearance for Neural Radiance Fields. In: Proceedings of the IEEE/CVF Conference on Computer Vision and Pattern Recognition
- Voynov O, Bobrovskikh G, Karpyshev P, et al (2023) Multi-sensor large-scale dataset for multi-view 3D reconstruction. In: Proceedings of the IEEE/CVF Conference on Computer Vision and Pattern Recognition
- Wang F, Galliani S, Vogel C, et al (2021a) Patchmatchnet: Learned multi-view patch-match stereo. In: Proceedings of the IEEE/CVF Conference on Computer Vision and Pattern Recognition, pp 14194–14203
- Wang J, Wang P, Long X, et al (2022a) Neuris: Neural reconstruction of indoor scenes using normal priors. In: Proceedings of the 17th European Conference on Computer Vision, pp 139–155
- Wang P, Liu L, Liu Y, et al (2021b) NeuS: Learning Neural Implicit Surfaces by Volume Rendering for Multi-view Reconstruction. In: Proceedings of the 35th Annual Conference on Neural Information Processing Systems
- Wang X, Fouhey D, Gupta A (2015) Designing deep networks for surface normal estimation. In: Proceedings of the IEEE Conference on Computer Vision and Pattern Recognition, pp 539–547
- Wang Y, Skorokhodov I, Wonka P (2022b) Hf-neus: Improved surface reconstruction using high-frequency details. *Advances in Neural Information Processing Systems* 35:1966–1978
- Wang Y, Han Q, Habermann M, et al (2023a) Neus2: Fast learning of neural implicit surfaces for multi-view reconstruction. In: Proceedings of the 19th IEEE/CVF International Conference on Computer Vision, pp 3295–3306
- Wang Y, Skorokhodov I, Wonka P (2023b) PET-Neus: Positional Encoding Triplanes for Neural Surfaces. In: Proceedings of the IEEE/CVF Conference on Computer Vision and Pattern Recognition
- Wei X, Li Z, Ding B, et al (2025) Revisiting Supervised Learning-Based Photometric Stereo Networks. *IEEE Transactions on Pattern Analysis and Machine Intelligence*
- Woodham RJ (1980) Photometric method for determining surface orientation from multiple images. *Optical Engineering* 19(1):139–144
- Wu L, Ganesh A, Shi B, et al (2011) Robust photometric stereo via low-rank matrix completion and recovery. In: Proceedings of the 10th Asian Conference on Computer Vision, pp 703–717
- Xu Q, Kong W, Tao W, et al (2022) Multi-scale geometric consistency guided and planar prior assisted multi-view stereo. *IEEE Transactions on Pattern Analysis and Machine Intelligence* 45(4):4945–4963
- Yang W, Chen G, Chen C, et al (2022) PS-NeRF: Neural Inverse Rendering for Multi-view Photometric Stereo. In: Proceedings of the 17th European Conference on Computer Vision, pp 266–284

- Yang X, Yuan L, Wilber K, et al (2024) Polymax: General dense prediction with mask transformer. In: Proceedings of the IEEE/CVF Winter Conference on Applications of Computer Vision, pp 1050–1061
- Yao Y, Luo Z, Li S, et al (2018) Mvsnet: Depth inference for unstructured multi-view stereo. In: Proceedings of the 15th European Conference on Computer Vision, pp 767–783
- Yariv L, Kasten Y, Moran D, et al (2020) Multi-view Neural Surface Reconstruction by Disentangling Geometry and Appearance. *Advances in Neural Information Processing Systems* 33:2492–2502
- Yariv L, Gu J, Kasten Y, et al (2021) Volume rendering of neural implicit surfaces. In: Proceedings of the 35th Annual Conference on Neural Information Processing Systems
- Ye C, Qiu L, Gu X, et al (2024) StableNormal: Reducing Diffusion Variance for Stable and Sharp Normal. *ACM Transactions on Graphics* 43(6):1–18
- Yu Y, Meka A, Elgharib M, et al (2020) Self-supervised outdoor scene relighting. In: Proceedings of the 18th European Conference on Computer Vision, pp 84–101
- Yu Z, Peng S, Niemeyer M, et al (2022) Monosdf: Exploring monocular geometric cues for neural implicit surface reconstruction. *Advances in Neural Information Processing Systems* 35:25018–25032
- Zhang J, Yao Y, Li S, et al (2022) Critical regularizations for neural surface reconstruction in the wild. In: Proceedings of the IEEE/CVF Conference on Computer Vision and Pattern Recognition, pp 6270–6279
- Zhang J, Li S, Luo Z, et al (2023a) Vis-mvsnet: Visibility-aware multi-view stereo network. *International Journal of Computer Vision* 131(1):199–214
- Zhang Y, Hu Z, Wu H, et al (2023b) Towards unbiased volume rendering of neural implicit surfaces with geometry priors. In: Proceedings of the IEEE/CVF Conference on Computer Vision and Pattern Recognition, pp 4359–4368
- Zhao D, Lichy D, Perrin PN, et al (2023) MVPSNet: Fast Generalizable Multi-view Photometric Stereo. In: Proceedings of the 19th IEEE/CVF International Conference on Computer Vision, pp 12525–12536